

THESIS

DESIGN AND EVALUATION OF AN INSTRUMENTED MICROFLUIDIC ORGANOTYPIC
DEVICE AND SENSOR MODULE FOR ORGAN-ON-A-CHIP APPLICATIONS

Submitted by

Alec Evan Richardson

School of Biomedical Engineering

In partial fulfillment of the requirements

For the Degree of Master of Science

Colorado State University

Fort Collins, Colorado

Summer 2020

Master's Committee:

Advisor: Charles Henry
Co-Advisor: Stuart Tobet

David Bark
Zaid Abdo

Copyright by Alec Evan Richardson 2020

All Rights Reserved

ABSTRACT

DESIGN AND EVALUATION OF AN INSTRUMENTED MICROFLUIDIC ORGANOTYPIC DEVICE AND SENSOR MODULE FOR ORGAN-ON-A-CHIP APPLICATIONS

Organ and tissue-on-a-chip technologies are powerful tools for drug discovery and disease modeling, yet many of these systems rely heavily on *in vitro* cell culture to create reductionist models of tissues and organs. Therefore, Organ-on-chip devices recapitulate some tissue functions and are useful for high-throughput screening but fail to capture the richness of cellular interactions of tissues *in vivo* because they lack the cellular diversity and complex architecture of native tissue. This thesis describes the design and testing of 1) a microfluidic organotypic device (MOD) for culture of murine intestinal tissue and 2) a microfluidic sensor module to be implemented inline with the MOD for real-time sensing of analytes and metabolites. The MOD houses full-thickness murine intestinal tissue, including muscular, neural, immune, and epithelial components. We used the MOD system to maintain murine intestinal explants for 72 h *ex vivo*. Explants cultured in the MOD formed a barrier between independent fluidic channels perfused with media, which is critical to recapitulating intestinal barrier function *in vivo*. We also established differential oxygen concentrations in the fluidic channels and showed that more bacteria were present on the tissue's mucosal surface when exposed to near-anoxic media. The sensor module is a reversibly sealed microfluidic device with magnetic connections that can withstand high backpressures. Further, electrodes housed in commercial finger-tight fittings were integrated into the sensor module in a plug-and-play format. Future work will include developing electrochemical/optical sensors for various biological compounds relevant to intestinal physiology. Ultimately, the MOD and sensor

module will be implemented in long-term microbiome studies to elucidate the relationship among microbial, epithelial, neuro and immune components of the gut wall in health and disease.

ACKNOWLEDGEMENTS

This thesis would not have been possible without the support of many people. First and foremost, I want to thank my advisor Chuck Henry and Co-advisor Stu Tobet for believing in me and giving me a chance to contribute to the scientific community. In addition to valuing my research contributions, they invested much of their time towards my personal and professional development. I thank my committee members Dave Bark and Zaid Abdo for their encouragement and support. Dave, your biofluid mechanics class was a great resource for many of the technical aspects of my project.

I would also like to thank my colleague and good friend, Luke Schwerdtfeger. I have had the pleasure of knowing Luke for 3 years, and my project would not have succeeded without his contributions as a skilled biologist. I will always have fond memories of our pre-experiment Chance the Rapper sessions, lunches at Paninos, and unforgettable nights at Pinball Jones. Cheers to always staying “on a path”, ole’ sport. During my time at CSU, I also became great friends with several of my lab mates who, in many ways, felt like a second family. They were individuals I could not only confide in when my experiments had failed for the thousandth time, but also celebrate with when I finally succeeded.

Lastly, I would like to thank my family for their unwavering support of my ambitions, regardless of how they changed over time. Thank you for enduring all my anxieties and uncertainties while reassuring me that I am, indeed, intelligent and hardworking. Ultimately, I’m certain that you’ll be there for me when no one else is. Family over everything. I love you, always.

TABLE OF CONTENTS

ABSTRACT	ii
ACKNOWLEDGEMENTS	iv
CHAPTER 1. INTRODUCTION	1
1.1 Organ-on-a-Chip Technologies and Applications	1
1.2 The Intestine’s Role in Human Health and Disease	4
1.2.1 Anatomy and Physiology.....	4
1.2.2 Host Tissue-Microbiome Interactions	6
1.3 Devices for Modeling Intestinal Physiology	9
1.3.1 The Ussing Chamber	9
1.3.2 Gut-on-a-Chip	12
1.4 Design Considerations for an Ex Vivo Intestinal Model	15
1.4.1 Materials and Manufacturing	15
1.4.2 On-Chip Microenvironment	16
1.4.3 Quantification of Tissue Health and Barrier Integrity	18
1.4.4 Real-Time Sensing of Analytes and Metabolites	21
REFERENCES	25
CHAPTER 2. A MICROFLUIDIC ORGANOTYPIC DEVICE FOR CULTURE OF MAMALLIAN INTESTINE EX VIVO	30
2.1 Summary.....	30
2.2 Introduction	30

2.3 Methods	32
2.4 Results and Discussion	37
2.5 Conclusion	42
REFERENCES	43
CHAPTER 3. A MAGNETICALLY ASSEMBLED MICROFLUIDIC SENSOR MODULE FOR ORGAN-ON-A-CHIP SYSTEMS	46
3.1 Introduction	46
3.2 Methods	48
3.3 Results and Discussion	52
3.4 Conclusion	54
REFERENCES	56
CHAPTER 4. CONCLUSION AND FUTURE DIRECTIONS	58
REFERENCES	61
APPENDIX A: 2019 MICROTAS CONFERENCE PAPER	62
APPENDIX B: COMPUTATIONAL MODEL OF INTESTINAL OXYGEN TRANSPORT WITHIN A MICROFLUIDIC ORGANOTYPIC DEVICE	66

CHAPTER 1. INTRODUCTION

1.1 Organ-on-a-Chip Technologies and Applications

Since its advent in the early 20th century, traditional in vitro cell culture has proven to be instrumental in disease modeling and pharmaceutical drug development. Cell lines are typically cultured in static environments such as petri dishes or Transwell inserts and are utilized in areas ranging from cancer research to vaccine manufacturing and monoclonal antibody production.¹ Within the field of pharmaceutical drug research, specifically, in vitro cell culture is implemented in preclinical studies, relying on high-throughput screening (HTS) to rapidly access tens to hundreds of thousands of potential drug candidates for cytotoxic effects and their ability to modulate a biological target of interest.² HTS is advantageous because it accelerates the preclinical drug development timeline and reduces costs associated with large sample volumes.² However, HTS is often carried out in multi-well plates containing confluent 2D cell monolayers, thus lacking physiological fluid flow, 3D architecture, and complex cellular interactions.^{3,4} As a result, data acquired from 2D cell culture models may not reflect the results of in vivo studies or clinical trials due to differences in the biological response to a compound of interest. Nearly 95% of all compounds reaching clinical trials in the drug development pipeline ultimately fail, which costs pharmaceutical companies years of research and billions in USD.⁵ The high failure rate of drugs entering clinical trials can be attributed to a variety of factors such as irreproducibility, poor safety profiles, and differences in drug efficacy on cultured cells versus animals or humans.⁵

To improve translation between in vitro models and clinical trials, Organ-on-a-Chip (OOC) technologies have emerged and quickly evolved over the last two decades. OOC devices integrate in vitro cell culture with microfluidic platforms to recapitulate complex organ-level physiology. While Schuler and colleagues were first to mimic organ-level physiology in a microfluidic device

in 2004,⁶ the term “Organ-on-a-Chip” was popularized by Donald Ingber in 2010 after developing the Lung-on-a-Chip,⁷ shown in Figure 1.1. The device consists of a cell-laden porous membrane placed between two polydimethylsiloxane (PDMS) layers containing microchannels and chambers for fluid flow and vacuum application, respectively. Epithelial and endothelial cells cover opposing sides of the porous membrane to represent the alveolus-capillary interface in the lungs. Chambers adjacent to the membrane deform upon cyclic vacuum application, mechanically stretching the porous membrane to simulate breathing-induced deformation of the alveolus-capillary interface. Incorporating mechanical deformation into the model significantly altered the cells’ physiological response to various perturbations. As an example, the introduction of silica nanoparticles to the alveolar channel in conjunction with mechanical strain drastically upregulated expression of the transmembrane protein, ICAM-1, increasing neutrophil adhesion to endothelial cells.⁷ By providing physiological biomechanical cues, *in vitro* organ models more closely

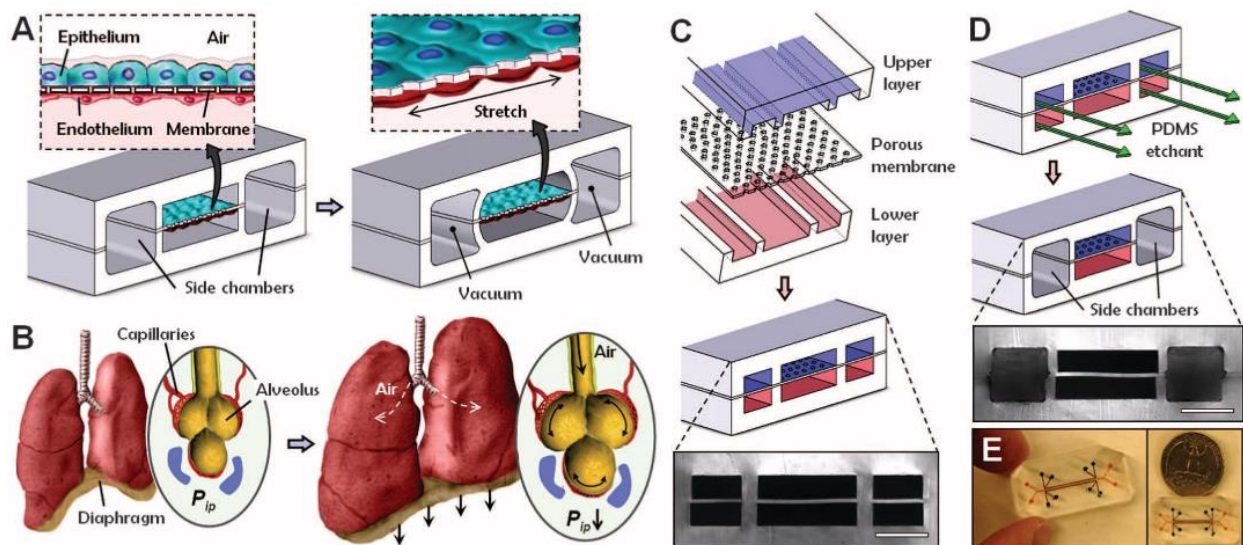


Figure 1.1 Schematic of the Lung-on-a-Chip illustrating the working principles and chip design. The chip simulates alveolus-capillary physiology by mimicking the air-liquid interface across epithelial and endothelial cell layers and providing cyclic strain. A) Vacuum suction provides cyclic strain to the epithelial monolayer. B) Mechanical strain induced on lung tissue *in vivo* when breathing. C) Layers of the Lung-on-a-Chip. D) Fabrication of the side chambers. E) Images of an actual Lung-on-a-Chip device. Reproduced from ref. 7 with permission from the The American Association for the Advancement of Science.

represent their in vivo counterparts.⁸ In addition to the lungs, organs such as the brain,⁹ kidneys,¹⁰ liver,¹¹ heart,¹² intestines,¹³ and many others have been modeled in microfluidic devices. Further, multiple organs have been combined in a single microfluidic platform to create Body-on-a-Chip devices capable of modeling systemic physiology.^{14,15}

While most OOC devices rely on one or more cell lines to represent tissues and organs, several research groups have taken an alternative approach by utilizing tissue explants or precision cut tissue slices for ex vivo organ models.¹⁶⁻¹⁸ Compared to cell lines, both tissue explants and slices are advantageous because they retain the cellular diversity, three-dimensional architecture, and function of native tissues.¹⁹ However, integrating explants and slices into microfluidic devices presents challenges such as long-term tissue viability, inadequate nutrient diffusion through the tissue, and limited source availability.¹⁹ Thus, both approaches to modeling organ level physiology in OOC devices are necessary to bridge the gap between HTS and clinical trials. For OOC technologies to become widely adopted in the pharmaceutical industry as preclinical tools, protocols must be established outlining standard operating procedures and validation methods.²⁰ Additionally, factors such as cell/tissue variability, scalable manufacturing, and quantitative data extraction will influence OOC utility in the drug development pipeline.²⁰

OOC technologies are a promising tool for translational research and disease modeling. Within a decade, OOC's have evolved from one-off devices used exclusively in academic laboratories to commercialized products marketed to large pharmaceutical companies. While 2D cell monolayer cultures provide a necessary platform to rapidly screen many compounds in parallel, they fail to adequately predict a drug's effect in vivo. OOC systems more faithfully recapitulate in vivo physiology, making them an attractive middle ground between traditional in

vitro cell culture and in vivo studies. As OOC technologies become more standardized in the pharmaceutical industry, there will likely be a paradigm shift in the drug development pipeline.

1.2 The Intestine's Role in Human Health and Disease

1.2.1 Anatomy and Physiology

The intestines primarily function as a selective barrier by absorbing nutrients and water, excreting waste, and defending against harmful substances and pathogens. Partially digested food (chyme) enters the small intestine where critical nutrients such as sugars, amino acids, and fatty acids are absorbed into the bloodstream. Remaining luminal content is then moved to the large intestine via peristalsis to be dehydrated and excreted. To function as a selective barrier, intestinal tissue is multilayered and composed of epithelial, neural, immune, muscular, and vascular components. Additionally, a thick mucus layer covers the intestinal epithelium, serving as a first line of defense against dangerous pathogens.

As seen in Figure 1.2, the small intestine's mucosal layer faces the lumen and contains three-dimensional finger-like structures (villi) lined by epithelial cells (e.g. enterocytes, goblet, Paneth), which increases surface area and improves nutrient absorption. Epithelial cells are connected to each other via tight junction proteins that prevent transcellular penetration of pathogens and other harmful substances. In diseased states, these tight junction proteins loosen, resulting in increased intestinal permeability. Intestinal glands, known as crypts, are located adjacent to the villi and contain several cell types, including stem cells. In humans, the intestinal epithelium is regenerated every 3-5 days as stem cells differentiate into epithelial cells and migrate apically up the crypt-villus axis.²¹ The mucosal layer also includes an extensive number of innate and adaptive immune cells within the lamina propria such as T cells, B cells, and dendritic cells.

Further, both vascular and neuronal components traverse all layers of the intestine and function synergistically with immune and epithelial cells to maintain homeostasis and regulate barrier function.²² As mentioned earlier, the intestines pass contents through the alimentary canal via segmental muscle contractions known as peristalsis. Within the intestinal muscle layer, two distinct muscle fiber orientations exist to enable peristaltic contractions: circular and longitudinal. Beneath the muscle layers, a lubricating serous membrane encapsulates the intestines to reduce friction against other organs. The intestine's unique microenvironment, namely the presence of a steep oxygen gradient across the epithelial layer, distinguishes it from other barrier tissues. Oxygen tensions precipitously transition from 0.1-1 mmHg to 80-100 mmHg as one moves from the lumen to submucosa.²⁴ Blood flow in the submucosal vasculature sufficiently oxygenates intestinal

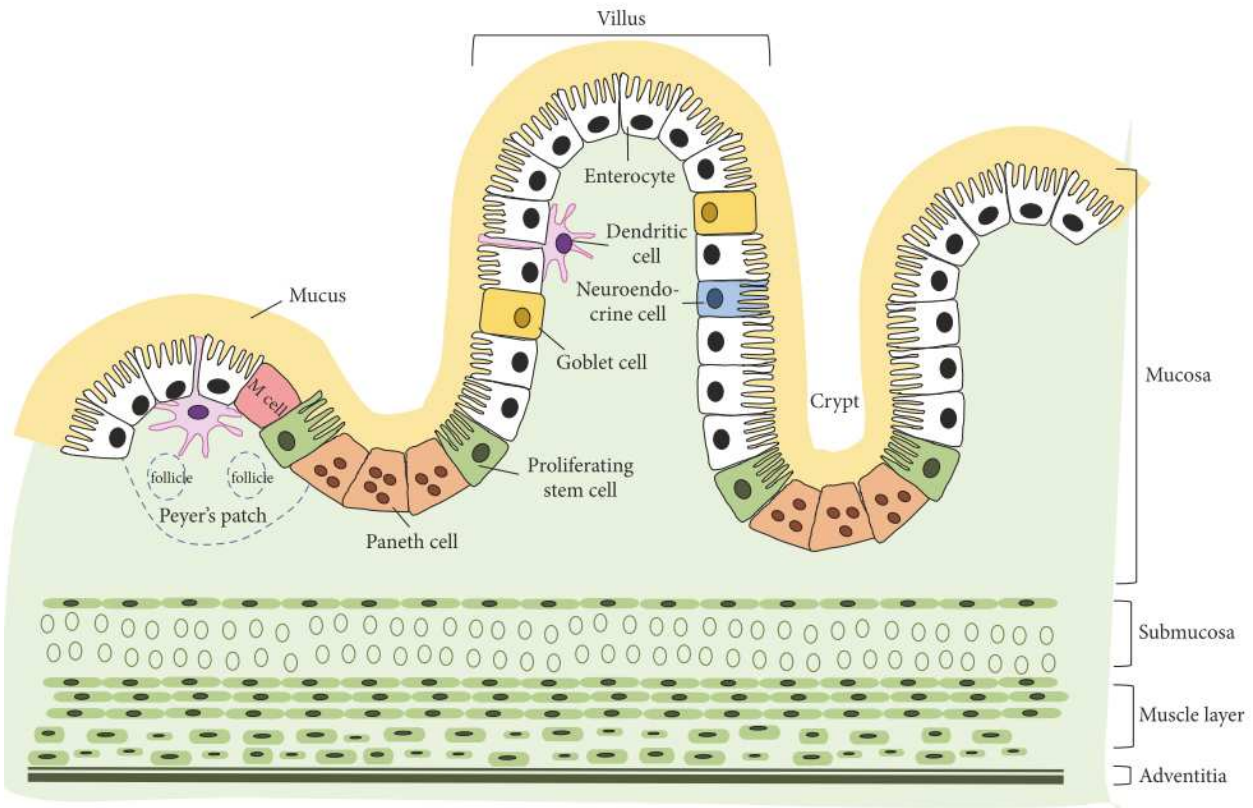


Figure 1.2 Cross sectional schematic illustrating the 4 main intestinal layers: Mucosa, Submucosa, Muscle, and Adventitia/Serosa. The mucosal layer features a wide range of epithelial cells organized in 3D structures. Reproduced from ref. 23

tissue while lower oxygen concentrations maintain anaerobic bacterial populations in the lumen. The next section will further explore the relationship between host tissue, the intestinal microbiome, and human health and disease.

1.2.2 Host Tissue-Microbiome Interactions

The adult human gastrointestinal (GI) tract is home to trillions of bacteria spanning roughly ~2000 individual species.²⁵ Gut bacteria continuously communicate with each other and host tissue to modulate energy levels, immune responses, and barrier function among other physiological processes.²⁶ For instance, bacteria metabolize undigested carbohydrates to produce the short chain fatty acids butyrate, propionate, and acetate, which act as signaling molecules to enhance tight junction formation between epithelial cells.²⁷ The distribution and abundance of bacterial species in the intestine is dependent on a variety of genetic, dietary, and environmental factors.²⁸ Research shows that changes in the gut microbiome, known as dysbiosis, are associated with a wide range of local and systemic diseases.²⁹ Studies that investigate the relationship between dysbiosis and disease typically rely on 16S rRNA sequencing of bacteria from cell cultures or fecal samples.³⁰ Thus, there is debate on the degree to which dysbiosis regulates disease pathogenesis and vice versa. In some germ-free mouse studies, the prevalence or severity of certain autoimmune diseases (e.g. type 1 diabetes, autoimmune arthritis) was reduced under germ-free conditions.²⁹ However, most studies have failed to link specific bacterial species to disease pathogenesis when isolated from the microbiome as a whole.²⁹

One of the most common intestinal diseases is inflammatory bowel disease (IBD), classified as either ulcerative colitis (UC) or Crohn's disease (CD). Both IBD subtypes are characterized by immune-mediated chronic inflammation of the intestine and are associated with unique microbial compositions.³¹ Studies analyzing biopsy or fecal bacterial profiles of IBD

patients have generally found increases in Enterobacteriaceae and decreases in microbial diversity, and some studies suggest these microbiome shifts precede or complement the onset of inflammation.³¹ As a complement to 16S rRNA sequencing, metabolic profiling of stool samples can elucidate some of the physiological mechanisms linking the gut microbiome to IBD. A recent study observed significant changes in metabolite abundance amongst UC and CD patients compared to controls, providing evidence that microbially-derived metabolites directly influence intestinal inflammation. As an example, IBD patients exhibited an overabundance of sphingolipids, a class of compounds present in both host cell and some bacterial cell membranes.³² Sphingolipid equilibrium is vital for maintaining intestinal homeostasis, and dysregulation in the metabolism/production of certain sphingolipid molecules is associated with IBD pathogenesis.³³ Despite advances in metabolomics and metagenomics, however, established relationships between dysbiosis, metabolic changes, and IBD are correlative rather than causative.

In addition to local diseases, research suggests the intestines play a significant role in the pathogenesis and progression of a variety of systemic diseases such as type 1 diabetes.³⁴ Type 1 diabetes is an autoimmune disorder characterized by T-cell mediated destruction of insulin-producing pancreatic β -cells, resulting in elevated blood glucose levels. Genetic factors associated with type 1 diabetes are well established, and a host of environmental factors (e.g. viruses, diet) are also proposed to increase susceptibility to the disease.³⁵ Considering the microbiome, several studies have observed increased Bacteroidetes/Firmicutes ratios, decreases in butyrate-producing bacteria, and decreased microbial diversity in type 1 diabetics.³⁶⁻³⁸ More recently, research suggests that gut bacteria are associated with type 1 diabetes pathogenesis via altered intestinal permeability and interactions with the innate and adaptive immune systems.³⁹ Illustrated in Figure 1.3, dysbiosis can increase intestinal permeability, allowing microbially-derived products to

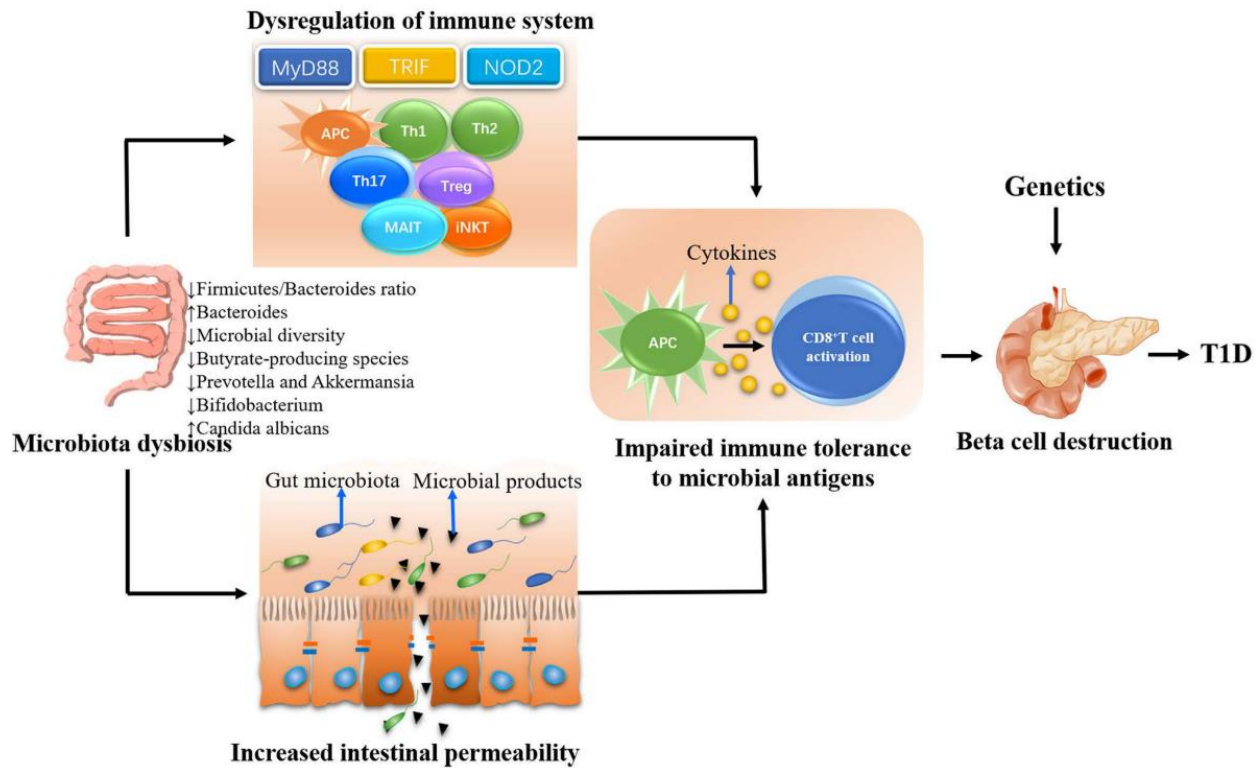


Figure 1.3 Proposed mechanisms by which intestinal bacteria contribute to the pathogenesis of Type 1 diabetes. Acronyms: MyD88 and TRIF are adaptor proteins; NOD2 is an intracellular pattern recognition receptor; APC is an antigen presenting cell; Th1, Th2, Th17 are T helper cells; Treg is a regulatory T cell; MAIT is a mucosal associated invariant T cell; iNKT are invariant natural killer T cells. Reproduced from ref. 40.

infiltrate host tissue unregulated.⁴⁰ In some cases, these products interact with enteric immune cells in a cascade of events ultimately leading to CD8⁺ T-cell activation and pancreatic β -cell destruction.⁴⁰ While these findings appear to confirm causal relationships between gut bacteria and type 1 diabetes, more large-scale human studies are needed to draw definitive conclusions.

The enteric nervous system (ENS) is intrinsic to the intestines and regulates key enteric functions such as motility, local blood flow, absorption/secretion, and immune responses.⁴¹ As the body's "second brain", the ENS continuously and bi-directionally communicates with the central nervous system (CNS) along the gut-brain axis via spinal afferents and the vagus nerve.⁴² Research has associated dysbiosis with neurological and mood disorders ranging from Alzheimer's disease to major depressive disorder,^{42,29} and the ENS provides a pathway for microbiome-brain

communication. More specifically, intestinal bacteria modulate the release of neuropeptides and other signaling molecules from enteric neurons and enteroendocrine cells, which in turn stimulates vagal and spinal afferent neurons leading to the brain.⁴³ Here, it should be noted that the ENS is only one component of the gut-brain axis and that certain signaling molecules produced by either bacteria or host cells can impact brain physiology directly via systemic circulation or by stimulating enteric immune cells.⁴³ Intestinal bacteria also produce and respond to several neurotransmitters known to impact mood, including gamma-amino butyrate (GABA), serotonin, dopamine, and norepinephrine.⁴⁴ Thus, dysbiosis alters the local availability of neurotransmitters and other neuroactive molecules absorbed by the intestines, ultimately impacting gut-brain communication.⁴⁴ However, neurotransmitters produced in the intestines may not reach the brain directly, and their modulation of the gut-brain axis is not well understood.²⁶

As evidenced in this section, the gut microbiome is associated with a growing number of local and systemic diseases through interactions with host tissue. 16S rRNA sequencing is a powerful method to identify and correlate microbial signatures with specific diseases, but a deeper understanding of the metabolites and pathways regulating host tissue-microbiome interactions is paramount for establishing causal relationships between dysbiosis and diseases. Though controversial, bacteriotherapy (i.e. fecal microbiota transplantation, probiotics) could become a viable treatment option for certain diseases in the future.²⁹ However, research must first elucidate what comprises a “healthy gut microbiome”, and it is likely that genetic/environmental factors will vary the therapy’s efficacy between individuals.²⁹

1.3 Devices for Modeling Intestinal Physiology

1.3.1 The Ussing Chamber

Since research has highlighted the critical role the intestines play in regulating human health, engineers and scientists have labored to design novel devices which enable recapitulation and analysis of intestinal physiology. The Ussing chamber, which was invented by Hans Ussing in the 1950's to study ion transport across frog skin, is a device widely-used to measure intestinal permeability and barrier function.⁴⁵ The classic Ussing chamber design, illustrated in Figure 1.4, consists of two buffer-filled acrylic half chambers separated by either intestinal mucosa or cultured epithelial cells. The buffer solution in each half chamber is maintained at a physiologic temperature and continuously gassed to 1) control dissolved O₂/CO₂ concentrations, and 2) stir the buffer for sufficient mixing. Further, most commercial systems are equipped with voltage-clamp/current-clamp setups which enable transepithelial electrical measurements such as resistance (R_{te}), voltage (V_{te}), and short-circuit current (I_{sc}).⁴⁶ In voltage-clamp experiments, “voltage electrodes” connected to each half chamber via salt bridges record V_{te} while “current-passing electrodes” in each half chamber pass current across the tissue. A feedback loop is used to automatically adjust

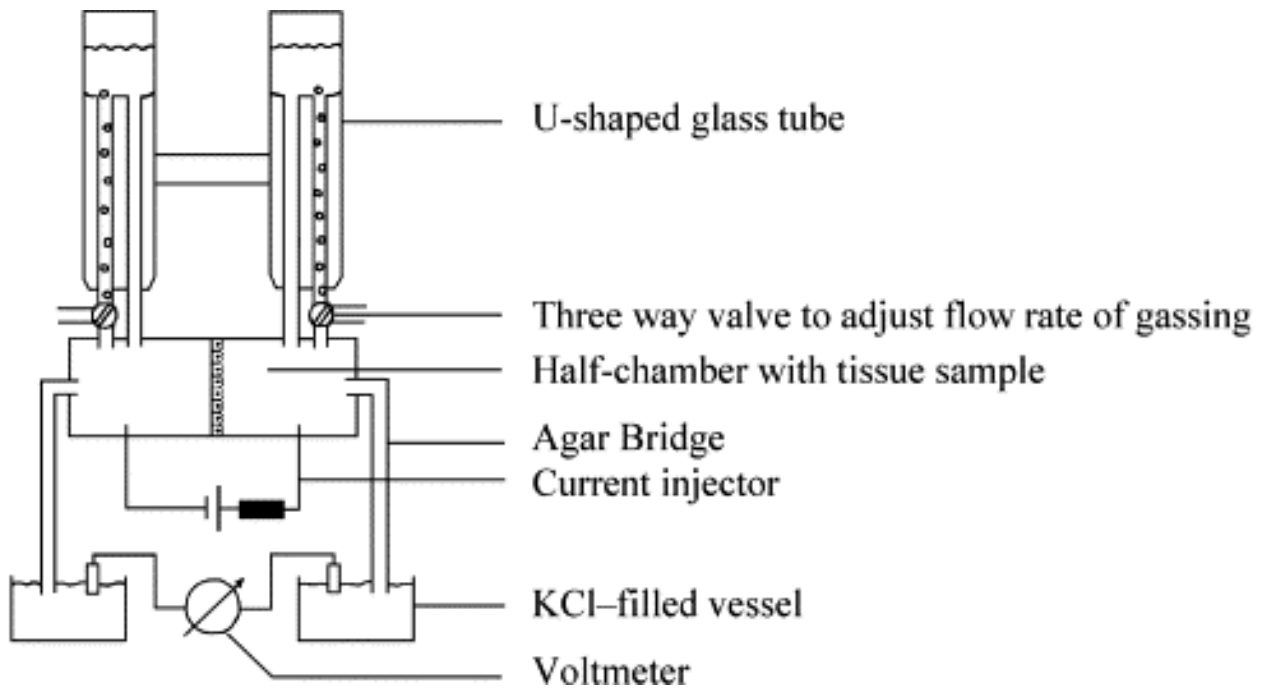


Figure 1.4 Schematic of the classical Ussing Chamber Design. Reproduced from ref. 46 with permission from Elsevier.

the applied current until the measured V_{te} matches a user-defined value (often 0V). Since V_{te} is constant, changes in the applied current are equal in magnitude and opposite in direction to ion transport through the tissue. The applied current is defined as I_{sc} when $V_{te}= 0V$. Compared to voltage-clamping, current-clamping involves injecting a constant current through the tissue and measuring fluctuations in V_{te} . Both techniques enable transepithelial electrical resistance (TEER) to be calculated from Ohm's law:

$$R_{te} = \frac{\Delta V}{\Delta I} \quad (1)$$

TEER, which will be further discussed in a later section, is a standard measure of tissue permeability and health.⁴⁷ Intestinal permeability to specific compounds can also be quantified in the Ussing chamber using bound radioactive or fluorescent probes.⁴⁸ Both half-chambers are sampled periodically after adding the labeled test compound, and intestinal permeability is calculated from the following equation:

$$P_{app} = \frac{dQ/dt}{SA * C_0} \quad (2)$$

Here, dQ/dt is the linear rate of transport between chambers, SA is the tissue's surface area, and C_0 is the initial concentration of the drug in the apical chamber.

The Ussing chamber offers several advantages compared to Transwell models of the intestinal barrier, including compatibility with explanted tissue, integrated instrumentation for electrophysiological measurements, and convection near the tissue's surfaces. While Ussing chamber studies have deepened our understanding of intestinal barrier function, many biological phenomena occur on timescales which exceed the device's capabilities. Ussing chambers are unsuited for long term microbiome studies and diseases models since tissue viability is limited to

3 hours.⁴⁸ The tissue's rapid degeneration likely stems from 1) physical damage induced when mounting the tissue between half chambers, and 2) exposure to buffer solutions lacking critical nutrients. The standard protocol for mounting tissue involves radially stretching the intestinal mucosa across the chamber's aperture, fastening the tissue's periphery to one half chamber via metal pins, and clamping both half-chambers together to prevent leakage.⁴⁸ While few studies have explored the effect of edge damage on bulk tissue health, one study showed that mounted ileal tissue segments exhibited altered villus morphology, cellular debris accumulation on the mucosal surface, and reduced mucosal thickness in regions adjacent to the chamber's edge.⁴⁹ Of concern, the authors noted that edge damage resulted in the inability to detect changes in transepithelial transport following exposure to hyperosmolar sodium chloride.⁴⁹

Modern commercial Ussing chambers are multiplexed and modular to increase throughput, improve usability, and reduce preparation time.^{45,48} Additionally, researchers have modified the classic chamber design to enable continuous perfusion or vacuum-assisted mounting of tissue segments,^{46,50} but no studies have directly investigated how various designs influence experiential results. The Ussing chamber remains the gold standard for studying transepithelial ion transport, and despite its limitations, has proven to be a valuable device for assessing intestinal barrier function *ex vivo*.

1.3.2 Gut-on-a-Chip

Gut-on-a-Chip is an OOC technology adapted to model intestinal epithelium *in vitro*. One of the earliest Gut-on-a-Chip designs,¹³ developed by Harvard University's Wyss Institute, is nearly identical to the Lung-on-a-Chip design⁷ and utilizes Caco-2 cells to represent the gut epithelium. Caco-2 cells are an established immortalized cell line for modeling intestinal permeability *in vitro*, but some of their functional characteristics differ from intestinal epithelial

cells *in vivo*.⁵¹ Further, while individual Caco-2 cells are morphologically similar to intestinal enterocytes,⁵¹ Caco-2 monolayers fail to capture the three-dimensional architecture and cellular diversity of the intestinal epithelium. However, Caco-2 monolayers cultured in the Gut-on-a-Chip developed villus-like structures in the presence of physiologic shear stress and mechanical strain, highlighting the impact of mechanical cues on tissue morphology.¹³ The physiological relevance of subsequent device iterations improved when Caco-2 monolayers were replaced with human small intestine-derived enteroids (intestinal organoids).⁵² The transcriptome of chips containing enteroids more closely matched that of human duodenum compared to chips containing Caco-2 cells.⁵² The most recent Gut-on-a-Chip design enables the establishment of transepithelial oxygen gradients between microfluidic channels and the coculture of host cells with intestinal anaerobic bacteria.⁵³ In this design, however, the epithelium is represented by Caco-2 cells instead of human-derived enteroids. In addition to the Gut-on-a-Chip, there are many other microfluidic intestinal models ranging in biological complexity. Table 1.1 compares the devices' design characteristics. Excluding *ex vivo* models, all microfluidic devices listed in Table 1.1 lack immune, nervous, and muscular components of the gut wall. To date, no microfluidic intestinal model completely captures the interaction between host tissue and the microbiome in a physiological environment.

As briefly discussed in section 1.1, several research groups have modeled organ physiology *ex vivo* by integrating tissue slices or explant into microfluidic systems. However, intestinal tissue is particularly difficult to culture in microfluidic devices because the tissue must form a barrier between opposing compartments, yet muscular contractions cause the tissue's periphery to curl towards its center axis. To the author's knowledge, only one research group has reported a microfluidic device for the culture of full-thickness intestinal explants.⁵⁶ Dawson et. al maintained full-thickness human intestinal explants (patients with IBD) for 72 h in a dual channel microfluidic

device providing continuous media perfusion. Explants were housed in a center PDMS chamber and petroleum jelly was applied around the tissue's periphery to prevent media from crossing channels. Tissue was considered viable after 72 h of culture by assessing tissue architecture (H&E stain) and quantifying lactate dehydrogenase release and cell proliferation (Ki-67 stain). However, we challenge the authors' claim that tissue was viable after 72 h because H&E stains of the explants at 72 h versus 0 h were markedly different. While use of intestinal explants better reflects host tissue dynamics, antibiotics added to the culture media precluded studies of host tissue-microbiome interactions.

Table 1.1 Comparison of various static and microfluidic models of the intestines. Adapted from ref. 54.

Model	TEER	Absorption	Coculture	Microbiome	Differentiation	Peristalsis	Drug Metabolism	Crypt-villus axis	Oxygen modulation	Disease modeling
<u>Static</u>										
Transwell	Yes ⁷⁶	Yes ^{76,77}	No	Yes ^{78,79}	No	No	No	No	No	No
Organoid	No	Yes ⁸⁰	No	Yes ⁸¹	Yes ⁸²	No	Yes ⁸³	Yes ⁸²	No	Yes ⁸⁴
Ex vivo	Yes ^{85,86}	Yes ^{85,87}	No	Yes ⁸³	Yes ⁸⁵	No	Yes ⁸⁸	Yes ⁸⁵	Yes ⁸⁹	Yes ⁸⁶
Scaffold	No	No	No	No	Yes ⁹⁰	No	No	Yes ⁹⁰	No	No
<u>Microfluidic</u>										
2-channel	Yes ⁶⁷	Yes ⁹¹	Yes ⁹²	No	No	No	Yes ⁹³	Yes ⁹³	No	No
Ex vivo	No	Yes ⁸⁹	No	No	Yes ⁵⁵	No	No	Yes ⁵⁵	No	Yes ⁵⁵
Multichannel (HuMiX)	Yes ⁹⁴	No	No	Yes ⁹⁴	No	No	No	No	Yes ⁹⁴	No
Gut Chip	Yes ^{13,95}	Yes ¹³	No	Yes ^{13,95}	Yes ^{95,96}	Yes ^{13,95,96}	Yes ^{13,96}	Yes ^{13,95,96}	No	Yes ⁹⁵

In conclusion, microfluidic devices can be used to model intestinal physiology both in vitro and ex vivo. Unlike static systems, microfluidic devices enable constant nutrient delivery and waste removal from cells and tissues.¹⁹ In vitro systems like the Gut-on-a-Chip are valuable for higher throughput studies and reflect the dynamics of native intestinal tissue to some degree, but they lack necessary aspects of the gut wall. Ex vivo microfluidic intestinal models capture the cellular diversity and three-dimensional architecture of native tissue, but limited tissue viability and availability have prevented their wide-spread use. Ideally, the next generation of microfluidic

intestinal models will contain all components of the gut wall and enable researchers to study host tissue-microbiome interactions in relation to human health and disease.

1.4 Design Considerations for an Ex Vivo Intestinal Model

1.4.1 Material and Manufacturing

PDMS is an elastomeric polymer widely used to fabricate microfluidic chips and OOC devices since it is relatively inexpensive, easy to fabricate, optically transparent, and bonds to an array of substrates.¹⁹ Despite these advantages, certain PDMS material properties are problematic when designing a microfluidic device to model the intestines. Physiologically relevant intestinal models require a near-anoxic environment near the tissue's mucosal surface, but PDMS's high oxygen permeability allows oxygen to readily diffuse from the surrounding environment into culture media.⁵⁶ In fact, Shin et al. accounted for oxygen flux through PDMS to accurately model oxygen transport in a microfluidic device lined with intestinal epithelial cells. Another drawback to PDMS is that it absorbs small hydrophobic molecules like pharmaceutical drugs.⁵⁷ When utilizing microfluidic devices for drug metabolism studies or bioassays, PDMS absorption of small molecules dilutes media drug concentrations and skews study results.⁵⁷ PDMS is not as ubiquitous in the OOC industry as it is in academic laboratories. Industrial OOC devices are typically fabricated from various thermoplastics such as polycarbonate, polystyrene, and polymethylmethacrylate.⁵⁸ Figure 1.5 compares materials commonly used to fabricate microfluidic devices and ranks their suitability for specific applications. Of the materials listed for tissue culture applications, cyclic olefin copolymer (COC) is well suited for ex vivo intestinal models because of its low oxygen permeability, minimal absorption of hydrophobic compounds, optical transparency, and biocompatibility.^{59,60} COC microfluidic chips can be fabricated via scalable manufacturing methods such as milling or injection-molding, which is critical for testing

multiple disposable microfluidic devices in parallel. By contrast, PDMS microfluidic devices are difficult to produce in mass quantities because fabrication requires manual labor and long curing times. While both milling and injection molding are viable manufacturing methods for plastic microfluidic devices, injection molding is more cost-effective as production volume increases despite high start-up costs.⁶¹ Additionally, the low shrinkage associated with injection molded COC provides engineers with more design flexibility. In conclusion, optimizing the design of an ex vivo intestinal model requires careful attention to material selection and manufacturing methods. COC is biocompatible and allows for low oxygen concentrations to be established on chip while injection-molding enables high volume production of parts at low costs long-term.

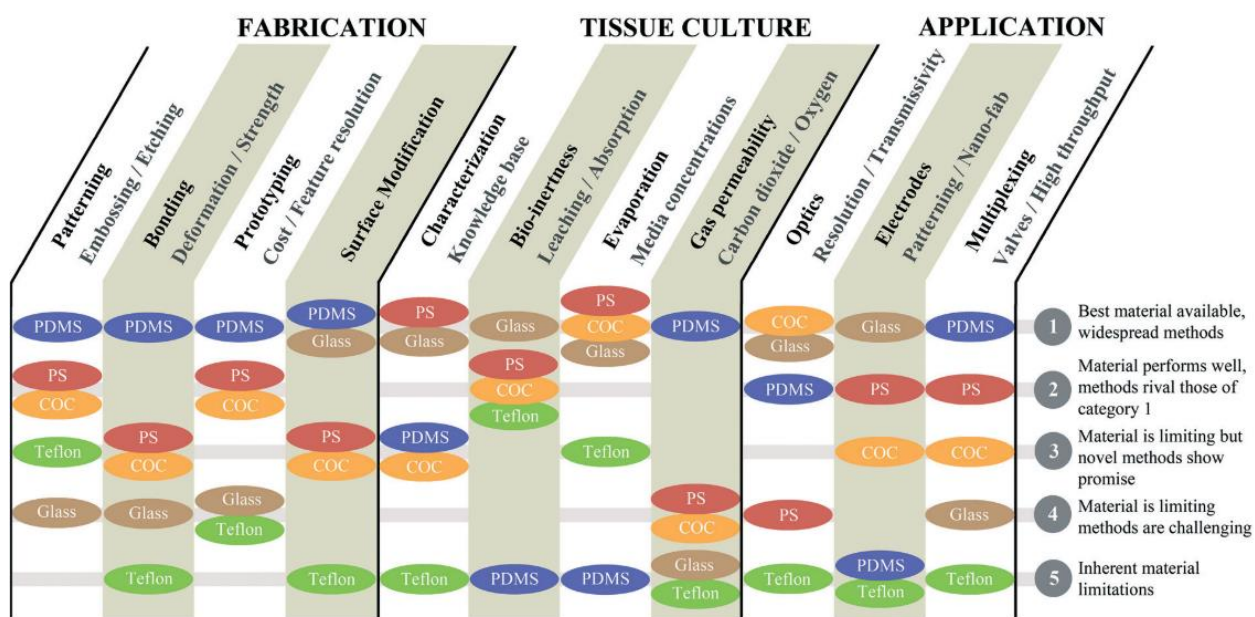


Figure 1.5 comparison of materials used to fabricate microfluidic devices for various applications. Acronyms: Polydimethylsiloxane (PDMS); Polystyrene (PS); Cyclic Olefin Copolymer (COC). Reproduced from ref. 19 with permission from the Royal Society of Chemistry.

1.4.2 On-Chip Microenvironment

The in vivo intestinal environment features dynamic physical and chemical characteristics which regulate homeostasis. Ex vivo intestinal models should capture this environment to maintain

viable tissue and demonstrate physiological relevance. One defining characteristic of the intestines is the presence of a steep oxygen gradient from the lumen to the serosa, which is necessary for the survival of both anaerobic bacteria and host tissue.²⁴ In vivo, this gradient is maintained by a combination of bacterial and tissue oxygen consumption, convective oxygen transport through vasculature, and diffusive oxygen transport from blood to surrounding tissues.⁶² Mathematically, this process is governed by the convection-diffusion equation as follows:

$$\frac{\partial c}{\partial t} = \nabla \cdot (D\nabla c) - \nabla \cdot (\mathbf{v}c) + R \quad (3)$$

where c is species concentration, D is the diffusion coefficient, \mathbf{v} is the velocity field of fluid carrying the species, and R is a reaction term accounting for species consumption or production. The del symbol ∇ acts as either the gradient operator (*i. e.* ∇c) or divergence operator (*i. e.* $\nabla \cdot (\mathbf{v}c)$). At steady state ($\partial c/\partial t = 0$), tissue oxygen consumption is equal to the combination of convective and diffusive oxygen transport. Since intestinal tissue lacks blood supply *ex vivo*, the concentration of oxygen within explants depends on boundary conditions at the mucosal and serosal surfaces. In microfluidic devices, tissue oxygenation is enhanced by establishing a larger concentration difference between channels and increasing flow rates. Experimentally measuring tissue oxygen levels while varying model parameters is challenging and time-consuming. However, computational modeling allows engineers to efficiently optimize model parameters such that oxygen distribution within intestinal explants is comparable to native tissue.

When optimizing perfusion flow rates for intestinal explants cultured in microfluidic devices, one must consider the magnitude of applied shear stress in addition to oxygen transport. In the context of fluid mechanics, shear stress is the component of stress acting parallel to a surface

in contact with moving fluid. For Newtonian fluids, shear stress (τ) is proportional to the shear rate ($\partial u/\partial y$) as shown in equation 4:

$$\tau = \mu \frac{\partial u}{\partial y} \quad (4)$$

where μ is the dynamic viscosity, u is fluid velocity, and y is the distance from fluid-wall interface. Shear stress serves an important role in many tissues and has been shown to modulate cell morphology and function in the intestines.⁶³ In vivo, the intestinal epithelium is subjected to low shear stresses ranging from .002-.08 dyne/cm² due to the movement of chyme along the GI tract.¹³ In microfluidic systems, the luminal flow rate should be adjusted to reflect physiologic shear stress values. Optimizing flow rates in the serosal channel is challenging because the intestinal serosa is not directly subjected to fluid flow in vivo. Rather, blood enters the serosa through mesentery arteries that are absent in ex vivo intestinal models.⁶⁴ Therefore, serosal flow rates should be optimized by 1) maximizing oxygen delivery to the tissue and 2) experimentally quantifying tissue health as a function of shear stress acting on the serosa.

While not extensively discussed in this section, the physiological relevance of an ex vivo intestinal model depends on other environmental parameters such as temperature, pH, and media composition. Ultimately, the on-chip microenvironment must recapitulate in vivo conditions for tissue and bacteria to survive long-term ex vivo.

1.4.3 Quantification of Tissue Health and Barrier Integrity

In organotypic slice cultures, tissue health is typically quantified using histological stains, immunohistochemistry, and cell-based assays.⁶⁵ Despite their utility, many of these techniques are implemented at the conclusion of experiments and do not provide real-time tissue health information. Barrier tissues such as the intestines are well-suited for non-invasive tissue health

analysis methods which include transepithelial electrical resistance (TEER) and quantifying paracellular flux of fluorescently labeled compounds. In addition to being non-invasive, these methods allow for real-time monitoring of barrier integrity.

TEER is a widely accepted, reliable measure of epithelial barrier integrity *in vitro*.⁴⁷ To obtain TEER values, electrodes are placed in opposing media filled compartments separated by an epithelial cell monolayer and a DC or AC voltage is applied. The measured current is converted to resistance or impedance values using Ohms law or equation 5, respectively.

$$Z = \frac{V(t)}{I(t)} = \frac{V_0 \sin \theta}{I_0 \sin (2\pi ft + \phi)} \quad (5)$$

Here, V_0 and I_0 are the peak voltage and current, θ is the phase shift, and f is the signal frequency. Resistance and impedance values reflect the integrity of tight junctions between cells, and TEER decreases as the epithelial barrier deteriorates. Impedance spectroscopy offers several advantages over traditional single frequency DC TEER measurements. Impedance values can be gathered over a wide range of frequencies, providing additional information such as cellular capacitance and membrane resistance.⁴⁷ Additionally, unlike DC currents, AC currents do not cause adverse effects on cells.⁶⁶ Figure 1.6 illustrates an equivalent circuit model for impedance measurements across an epithelial cell monolayer. In most systems, frequencies less than 100 Hz reflect TEER, 100 Hz-10 kHz reflects cell capacitance, and frequencies greater than 10 kHz reflect media resistance.⁶⁷ While TEER circuit models are well defined for cell monolayers, circuit models for tissue explants are less understood because of additional layers underlying the epithelium. When considering intestinal tissue specifically, one potential concern is that electrical resistance contributions from the submucosal and muscular layers may dominate the resistance contribution from the epithelial layer. Some studies have measured TEER across full-thickness explants, but the contributions of

each tissue layer to the total electrical resistance was not discussed. Detailed TEER circuit models for multilayered tissues are needed to correlate TEER fluctuations to tight junction dynamics. Whether TEER measurements are valid for multilayered tissues depends on future development and testing of TEER sensors in *ex vivo* systems.

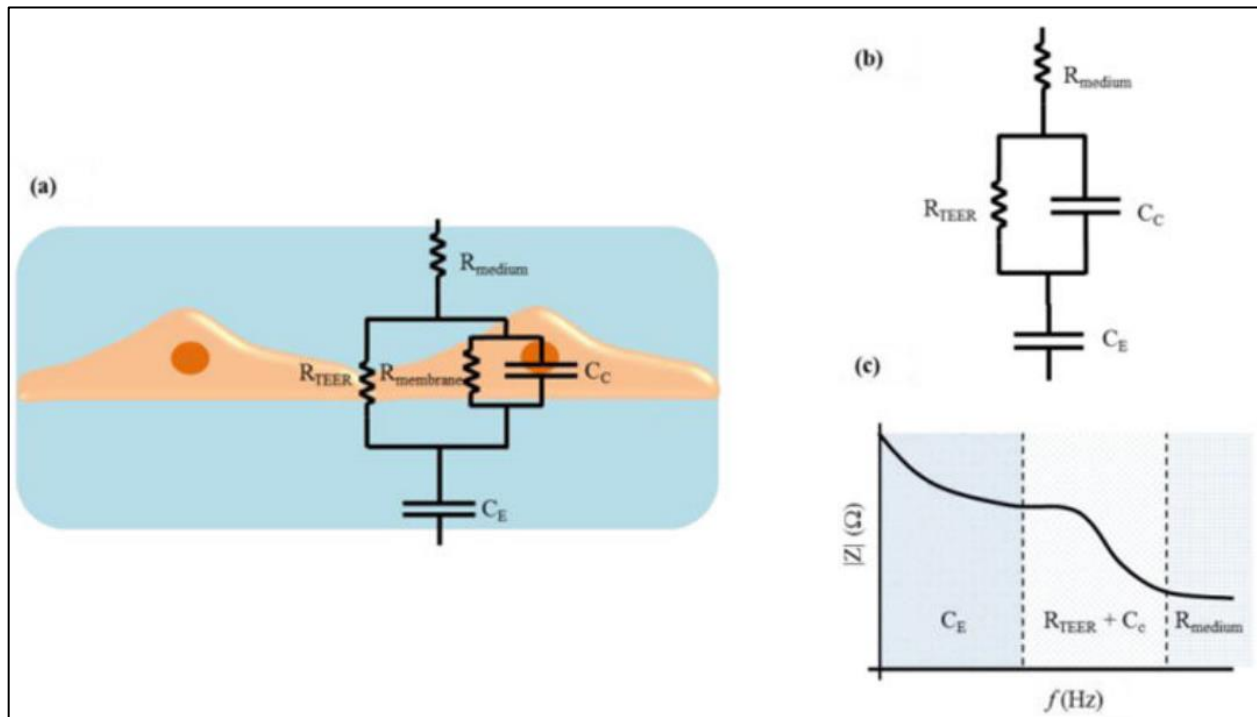


Figure 1.6 (a) and (b) show the equivalent circuit model for impedance measurements across epithelial cell monolayers. (c) correlates individual circuit elements to specific frequency ranges. Acronyms: R_{TEER} is transepithelial electrical resistance; R_{Medium} is medium resistance; $R_{Membrane}$ is membrane resistance; C_C is cell capacitance; C_E is electrode capacitance. Reproduced from ref. 47.

In addition to TEER, barrier integrity and tissue health can be quantified by monitoring the passage of fluorescently labeled compounds through tissues. This method yields specific information about paracellular spacing when using tracer compounds with defined molecular weights such as dextran (3-2000 kDa), mannitol (182 Da), and albumin (67 kDa) (Arik 2018). In static systems or Ussing chambers, media samples from each well or half chamber are taken periodically and assessed with a plate reader.^{48,68} The measured fluorescence intensity of each sample indicates the concentration of labeled compound. Optically transparent OOC devices,

when coupled with fluorescent microscopy, allow for real-time monitoring of compound concentration in the effluent media. For example, Adriani et. al. developed an OOC model of the blood-brain barrier and quantified endothelial permeability to labeled dextran by taking fluorescent images every minute.⁶⁹ When measuring paracellular flux in microfluidic devices, both the input compound concentration and media flow rates should be optimized so that the effluent media is concentrated enough to detect changes in flux over time.⁶⁸

Both TEER and paracellular flux measurements should be validated by traditional measures of tissue health and barrier integrity including tight junction protein expression and live/dead cell assays. Validation is crucial because TEER and paracellular flux measurements not only depend on tissue health/barrier integrity, but also device design, experimental setup, and tissue type. Overall, a well-designed ex vivo intestinal model should include methods for quantifying tissue health and barrier integrity in real-time to ensure that experimental results are physiologically relevant.

1.4.4 Real-Time Sensing of Analytes and Metabolites

On-chip sensors are increasingly becoming a standard feature of OOC devices due to advances in sensor development and chip fabrication.⁷⁰ Unlike off-chip assays, online sensing enables real-time monitoring of physical and biochemical parameters, which is crucial to understanding how tissues respond to environmental perturbations.⁷¹ On-chip sensors typically rely on electrochemical or optical sensing motifs, both of which have distinct advantages and limitations depending on the analyte being detected.

Electrochemical sensors are usually integrated into OOC devices by depositing and patterning metal electrodes on surfaces in contact with the microfluidic channels,⁷⁰ although other

electrode fabrication methods exist such as inkjet printing.⁷² Electrochemical sensors rely on redox reactions at the electrode's surface and the resulting signal is detected via potentiometric or amperometric methods.⁷¹ Enzymes are commonly incorporated into electrochemical sensors to increase selectivity for specific molecules like glucose, though poor enzyme stability can reduce the sensor's accuracy over time.⁷³ Further, electrochemical detection of amino acids, proteins, drugs, and many small molecules can be achieved by immobilizing antibodies or aptamers on the electrode's surface.⁷⁴ Electrochemical sensors are well-suited for OOC applications because they are easily fabricated, highly sensitive and selective, and relatively low cost.⁷¹ A recurrent challenge to electrochemically detecting analytes in complex culture medias is biofouling, whereby a fouling agent is passivated on the electrode surface.⁷⁵ However, biofouling can be reduced by applying electrode coatings or surface modifications.⁷⁵

In addition to electrochemical sensors, optical sensors can be readily integrated into OOC systems because of the high optical transparency of microfluidic devices. While many optical sensing motifs exist, this section will discuss optical sensors that rely on fluorescence intensity and lifetime measurements. For these types of optical sensors, polymeric thin films are doped with an analyte specific fluorescent dye and attached to either the inner surface of a microfluidic channel or to the tip of a fiber optic probe.⁷¹ For the first scenario, the polymeric thin film is interrogated remotely and non-invasively using the fiber optic probe. For the second scenario, the fiber optic probe must be in direct contact with culture media so that the attached thin film is exposed to the analyte of interest. In both cases, fluorescence quenching is directly related to the analyte concentration via the Stern-Volmer relationship (Chapter 2, equation 1). Although optical sensing methods are non-invasive and avoid analyte consumption, they are susceptible to photobleaching

and small changes in fiber optic probe positioning relative to the polymer film can significantly alter measurements.⁷¹

When considering the design of an ex vivo intestinal model, a microfluidic platform should accommodate both optical and electrochemical sensors in some capacity to maximize the range of detectable analytes and metabolites. However, the compact size of microfluidic devices limits the number of sensors that can be integrated into a single chip. One solution is to integrate additional sensors into microfluidic devices in line with the device housing tissue. Indeed, on-chip sensors could be reserved for monitoring the intestinal microenvironment (i.e. oxygen, pH) while downstream sensors could be used to detect analytes associated with tissue and microbial metabolism (i.e. glucose, lactate). Since the intestines are comprised of epithelial, neural, immune, muscular, vascular, and microbial components, there are a multitude of analytes relevant to intestinal physiology, many of which are summarized in Table 1.2. Sensing each of these analytes in real-time from one tissue sample is a formidable endeavor. However, by collecting effluent media in fractions over time, many of these analytes could be measured at the conclusion of experiments via mass spectrometry or other analytical techniques. Additionally, multiplexing tissue chips would allow experimenters to sense various analytes from different tissue samples. Ultimately, the type and number of sensors used in any given experiment will depend on the biological questions being asked.

Table 1.2: Sensing methods for analytes and metabolites relevant to intestinal physiology

Target	Detection Method (Electrochemical or Optical)	Goal
Oxygen	Both	Monitor consumption in both channels
Lactate	Both*	Monitor cellular metabolism
Lactate Dehydrogenase	Unknown	Monitor cell death
Glucose	Both*	Monitor nutrient consumption/metabolism
pH	Both ⁺	Monitor metabolism
Short Chain Fatty Acids	NMR (short term) Both ⁺ (long term)	Monitor microbiome outputs
Trimethylamine	Electrochemical ⁺	Assess microbial output
Serotonin (5-HT)	Electrochemical ⁺	Monitor enterochromaffin and neural output into lumen
Kynurenine	ELISA (short term)	Assess alternate and more plentiful tryptophan metabolite
Neuropeptides (e.g. VIP)	Electrochemical ⁺	Assess neurosecretion that might reach either microfluidic compartment
Cytokines	ELISA (short term) Electrochemical ⁺ (long term)	Monitor immune and epithelial cellular outputs
Matrix Metalloproteinases	ELISA (short term) Electrochemical ⁺ (long term)	Monitor cellular output to quantify inflammatory response
Muc2/GalNaz	Optical ⁺	Monitor mucus sloughing
Eicosanoids (PGE2)	ELISA	Assess cox1/2 inhibition by NSAIDs
Defensin(s)	ELISA (short term) Electrochemical ⁺ (long term)	Assess Paneth cell secretion

* requires enzymatic surface modification

⁺ requires non-enzymatic surface modification

REFERENCES

1. O. O. Oyeleye, S. T. Ogundeji, S. I. Ola and O. G. Omitogun, *Biotechnol. Mol. Biol. Rev.*, 2016, **11**, 6–16.
2. D. A. Pereira and J. A. Williams, *Br. J. Pharmacol.*, 2007, **152**, 53–61.
3. P. Szymański, M. Markowicz and E. Mikiciuk-Olasik, *Int. J. Mol. Sci.*, 2012, **13**, 427–452.
4. K. Jaroch, A. Jaroch and B. Bojko, *J. Pharm. Biomed. Anal.*, 2018, **147**, 297–312.
5. A. A. Seyhan, *Transl. Med. Commun.*, 2019, **4**, 1–19.
6. A. Sin, K. C. Chin, M. F. Jamil, Y. Kostov, G. Rao and M. L. Shuler, *Biotechnol. Prog.*, 2004, **20**, 338–345.
7. D. Huh, A. Matthews, Benjamin D. Mammoto, H. Y. Montoya-Zavala, Martín Hsin and D. E. Ingber, *Science (80-.)*, 2010, **328**, 1662–1668.
8. E. Ergir, B. Bachmann, H. Redl, G. Forte and P. Ertl, *Front. Physiol.*, 2018, **9**, 1–8.
9. N. R. Wevers, D. G. Kasi, T. Gray, K. J. Wilschut, B. Smith, R. Vught, F. Shimizu, Y. Sano, T. Kanda, G. Marsh, S. J. Trietsch, P. Vulto, H. L. Lanz and B. Obermeier, *Fluids Barriers CNS*, 2018, **15**, 1–12.
10. K. J. Jang, A. P. Mehr, G. A. Hamilton, L. A. McPartlin, S. Chung, K. Y. Suh and D. E. Ingber, *Integr. Biol. (United Kingdom)*, 2013, **5**, 1119–1129.
11. C. T. Ho, R. Z. Lin, W. Y. Chang, H. Y. Chang and C. H. Liu, *Lab Chip*, 2006, **6**, 724–734.
12. J. U. Lind, T. A. Busbee, A. D. Valentine, F. S. Pasqualini, H. Yuan, M. Yadid, S. J. Park, A. Kotikian, A. P. Nesmith, P. H. Campbell, J. J. Vlassak, J. A. Lewis and K. K. Parker, *Nat. Mater.*, 2017, **16**, 303–308.
13. H. J. Kim, D. Huh, G. Hamilton and D. E. Ingber, *Lab Chip*, 2012, **12**, 2165–2174.
14. I. Maschmeyer, A. K. Lorenz, K. Schimek, T. Hasenberg, A. P. Ramme, J. Hübner, M. Lindner, C. Drewell, S. Bauer, A. Thomas, N. S. Sambo, F. Sonntag, R. Lauster and U. Marx, *Lab Chip*, 2015, **15**, 2688–2699.
15. C. D. Edington, W. L. K. Chen, E. Geishecker, T. Kassis, L. R. Soenksen, B. M. Bhushan, D. Freake, J. Kirschner, C. Maass, N. Tsamandouras, J. Valdez, C. D. Cook, T. Parent, S. Snyder, J. Yu, E. Suter, M. Shockley, J. Velazquez, J. J. Velazquez, L. Stockdale, J. P. Papps, I. Lee, N. Vann, M. Gamboa, M. E. Labarge, Z. Zhong, X. Wang, L. A. Boyer, D. A. Lauffenburger, R. L. Carrier, C. Communal, S. R. Tannenbaum, C. L. Stokes, D. J. Hughes, G. Rohatgi, D. L. Trumper, M. Cirit and L. G. Griffith, *Sci. Rep.*, 2018, **8**.
16. P. M. Van Midwoud, M. T. Merema, E. Verpoorte and G. M. M. Groothuis, *Lab Chip*, 2010, **10**, 2778–2786.
17. X. Li and C. J. Easley, *Anal. Bioanal. Chem.*, 2018, **410**, 791–800.
18. A. E. Ross, M. C. Belanger, J. F. Woodroof, R. R. Pompano, *Analyst*, 2017, **142**, 649–659.
19. I. C. Mclean, L. A. Schwerdtfeger, S. A. Tobet and C. S. Henry, *Lab Chip*, 2018, 1399–1410.
20. B. Zhang, A. Korolj, B. F. L. Lai and M. Radisic, *Nat. Rev. Mater.*, 2018, **3**, 257–278.

21. A. S. Darwich, U. Aslam, D. M. Ashcroft and A. Rostami-Hodjegan, *Drug Metab. Dispos.*, 2014, **42**, 2016–2022.
22. B. B. Yoo and S. K. Mazmanian, *Immunity*, 2017, **46**, 910–926.
23. S. Kong, Y. H. Zhang and W. Zhang, *Biomed Res. Int.*, DOI:10.1155/2018/2819154.
24. M. G. Espey, *Free Radic. Biol. Med.*, 2013, **55**, 130–140.
25. A. Almeida, A. L. Mitchell, M. Boland, S. C. Forster, G. B. Gloor, A. Tarkowska, T. D. Lawley and R. D. Finn, *Nature*, 2019, **568**, 499–504.
26. M. H. Mohajeri, R. J. M. Brummer, R. A. Rastall, R. K. Weersma, H. J. M. Harmsen, M. Faas and M. Eggersdorfer, *Eur. J. Nutr.*, 2018, **57**, 1–14.
27. D. J. Morrison and T. Preston, *Gut Microbes*, 2016, **7**, 189–200.
28. E. Thursby and N. Juge, *Biochem. J.*, 2017, **474**, 1823–1836.
29. S. Carding, K. Verbeke, D. Vipond, B. Corfe and L. Owen, *Microb. Ecol. Heal. Dis.*, 2015, **26**, 26191-.
30. F. Backhed, R. E. Ley, J. L. Sonnenburg, D. A. Peterson and J. I. Gordon, *Science*, 2005, **307**, 1915–1919.
31. C. Huttenhower, A. D. Kostic and R. J. Xavier, *Immunity*, 2014, **40**, 843–854.
32. E. A. Franzosa, A. Sirota-Madi, J. Avila-Pacheco, N. Fornelos, H. J. Haiser, S. Reinker, T. Vatanen, A. B. Hall, H. Mallick, L. J. McIver, J. S. Sauk, R. G. Wilson, B. W. Stevens, J. M. Scott, K. Pierce, A. A. Deik, K. Bullock, F. Imhann, J. A. Porter, A. Zhernakova, J. Fu, R. K. Weersma, C. Wijmenga, C. B. Clish, H. Vlamakis, C. Huttenhower and R. J. Xavier, *Nat. Microbiol.*, 2019, **4**, 293–305.
33. L. A. Hadi, C. Di Vito and L. Riboni, *Mediators Inflamm.*, DOI:10.1155/2016/3827684.
34. J. A. Mullaney, J. E. Stephens, M. E. Costello, C. Fong, B. E. Geeling, P. G. Gavin, C. M. Wright, T. D. Spector, M. A. Brown and E. E. Hamilton-Williams, *Microbiome*, 2018, DOI:10.1186/s40168-018-0438-z.
35. K. M. Gillespie, *CMAJ*, 2006, **175**, 165–170.
36. A. Giongo, K. A. Gano, D. B. Crabb, N. Mukherjee, L. L. Novelo, G. Casella, J. C. Drew, J. Ilonen, M. Knip, H. Hyöty, R. Veijola, T. Simell, O. Simell, J. Neu, C. H. Wasserfall, D. Schatz, M. A. Atkinson and E. W. Triplett, *ISME J.*, 2011, **5**, 82–91.
37. C. T. Brown, A. G. Davis-Richardson, A. Giongo, K. A. Gano, D. B. Crabb, N. Mukherjee, G. Casella, J. C. Drew, J. Ilonen, M. Knip, H. Hyöty, R. Veijola, T. Simell, O. Simell, J. Neu, C. H. Wasserfall, D. Schatz, M. A. Atkinson and E. W. Triplett, *PLoS One*, 2011, **6**, 1–9.
38. P. F. De Groot, C. Belzer, Ö. Aydin, E. Levin, J. H. Levels, S. Aalvink, F. Boot, F. Holleman, D. H. Van Raalte, T. P. Scheithauer, S. Simsek, F. G. Schaap, S. W. M. Olde Damink, B. O. Roep, J. B. Hoekstra, W. M. De Vos and M. Nieuwdorp, *PLoS One*, 2017, **12**, 1–14.
39. P. Zheng, Z. Li and Z. Zhou, *Diabetes. Metab. Res. Rev.*, 2018, **34**, 1–9.

40. H. Zhou, L. Sun, S. Zhang, X. Zhao, X. Gang and G. Wang, *Front. Endocrinol.*, 2020, **11**, 1–13.
41. B. G. Nezami and S. Srinivasan, *Curr Gastroenterol Rep*, 2010, **12**, 358–365.
42. S. Ghaisas, J. Maher and A. Kanthasamy, *Pharmacol. Ther.*, 2016, **158**, 52–62.
43. P. Holzer and A. Farzi, *Adv. Exp. Med. Biol.*, 2014, **817**, 195–219.
44. L. Galland, *J. Med. Food*, 2014, **17**, 1261–1272.
45. J. Westerhout, H. Wortelboer and K. Verhoeckx, in *The Impact of Food Bioactives on Health: in vitro and ex vivo models*, Springer International Publishing, Cham, 2015, pp. 263–273.
46. H. Li, D. N. Sheppard and M. J. Hug, *J. Cyst. Fibros.*, 2004, **3**, 123–126.
47. J. J. Srinivasan, B.; Kolli, A.R.; Esch, M.B.; Abaci, H.E.; Shuler, L.; Hickman, B. Srinivasan, A. R. Kolli, M. B. Esch, H. E. Abaci, M. L. Shuler and J. J. Hickman, *J. Lab. Autom.*, 2015, **20**, 107–126.
48. L. L. Clarke, *Am J Physiol Gastrointest Liver Physiol*, 2009, 1151–1166.
49. B. H. Bajka, C. M. Gillespie, C. B. Steeb, L. C. Read and G. S. Howarth, *Scand. J. Gastroenterol.*, 2003, **38**, 732–741.
50. P. S. Osbak, N. Bindslev, S. S. Poulsen, N. Kaltoft, M. C. Tilotta and M. B. Hansen, *BMC Gastroenterol.*, 2007, DOI:10.1186/1471-230X-7-37.
51. T. Lea, in *The Impact of Food Bioactives on Health: in vitro and ex vivo models*, Springer International Publishing, Cham, 2015, 103–111.
52. M. Kasendra, A. Tovaglieri, A. Sontheimer-Phelps, S. Jalili-Firoozinezhad, A. Bein, A. Chalkiadaki, W. Scholl, C. Zhang, H. Rickner, C. A. Richmond, H. Li, D. T. Breault and D. E. Ingber, *Sci. Rep.*, 2018, **8**, 1–14.
53. W. Shin, A. Wu, M. W. Massidda, C. Foster, N. Thomas, D.-W. Lee, H. Koh, Y. Ju, J. Kim and H. J. Kim, *Front. Bioeng. Biotechnol.*, 2019, **7**, 1–13.
54. A. Bein, W. Shin, S. Jalili-firoozinezhad, M. H. Park, A. Sontheimer-phelps, A. Tovaglieri, A. Chalkiadaki, H. J. Kim and D. E. Ingber, *Cell. Mol. Gastroenterol. Hepatol.*, 2018, **5**, 659–668.
55. A. Dawson, C. Dyer, J. Macfie, J. Davies, L. Karsai, J. Greenman and M. Jacobsen, *Biomicrofluidics*, 2016, DOI:10.1063/1.4964813.
56. M. Hamon, S. Hanada, T. Fujii and Y. Sakaif, *Cell Transplant.*, 2012, **21**, 401–410.
57. B. J. van Meer, H. de Vries, K. S. A. Firth, J. van Weerd, L. G. J. Tertoolen, H. B. J. Karperien, P. Jonkheijm, C. Denning, A. P. IJzerman and C. L. Mummery, *Biochem. Biophys. Res. Commun.*, 2017, **482**, 323–328.
58. J. E. Sosa-Hernández, A. M. Villalba-Rodríguez, K. D. Romero-Castillo, M. A. Aguilar-Aguila-Isaías, I. E. García-Reyes, A. Hernández-Antonio, I. Ahmed, A. Sharma, R. Parra-Saldívar and H. M. N. Iqbal, *Micromachines*, 2018 , DOI:10.3390/mi9100536.

59. P. M. Van Midwoud, A. Janse, M. T. Merema, G. M. M. Groothuis and E. Verpoorte, *Anal. Chem.*, 2012, **84**, 3938–3944.
60. C. J. Ochs, J. Kasuya, A. Pavesi and R. D. Kamm, *Lab Chip*, 2014, **14**, 459–462.
61. D. J. Guckenberger, A. M. de Groot, Theodorus E. Wan, D. J. Beebe and E. W. K. Young, *Lab Chip*, 2015, **15**, 2364–2378.
62. L. Zheng, C. J. Kelly and S. P. Colgan, *Am J Physiol Cell Physiol.*, 2015, **309**, 350–360.
63. J. Costa and A. Ahluwalia, *Front. Bioeng. Biotechnol.*, 2019, **7**, 1–14.
64. D. N. Granger, P. D. I. Richardson, P. R. Kvietys and N. A. Mortillaro, *Gastroenterology*, 1980, **78**, 837–863.
65. S. Kallendrusch, J. Korfer, F. Lordick and I. Bechmann, *Integr. Cancer Sci. Ther.*, 2017, **4**, 1–5.
66. K. Benson, S. Cramer and H. J. Galla, *Fluids Barriers CNS*, 2013, **10**, 1–11.
67. O. Y. F. Henry, R. Villenave, M. J. Crouce, W. D. Leineweber, M. A. Benz and D. E. Ingber, *Lab Chip*, 2017, **17**, 2264–2271.
68. Y. B. Arlk, M. W. Van Der Helm, M. Odijk, L. I. Segerink, R. Passier, A. Van Den Berg and A. D. Van Der Meer, *Biomicrofluidics*, 2018, **12**, 1–13.
69. G. Adriani, D. Ma, A. Pavesi, R. D. Kamm and E. L. K. Goh, *Lab Chip*, 2017, **17**, 448–459.
70. B. Zhang, A. Korolj, B. F. L. Lai and M. Radisic, *Nat. Rev. Mater.*, 2018, **3**, 257–278.
71. T. Kilic, F. Navaee, F. Stradolini, P. Renaud and S. Carrara, *Microphysiological Syst.*, 2018, DOI:10.21037/mps.2018.01.01.
72. A. Moya, M. Ortega-Ribera, X. Guimerà, E. Sowade, M. Zea, X. Illa, E. Ramon, R. Villa, J. Gracia-Sancho and G. Gabriel, *Lab Chip*, 2018, **18**, 2023–2035.
73. N. Shen, H. Xu, W. Zhao, Y. Zhao and X. Zhang, *Sensors (Switzerland)*, 2019, DOI:10.3390/s19051203.
74. A. E. Radi, *Int. J. Electrochem.*, 2011, **2011**, 1–17.
75. B. L. Hanssen, S. Siraj and D. K. Y. Wong, *Rev. Anal. Chem.*, 2016, **35**, 1–28.
76. I. J. Hidalgo, T. J. Raub and R. T. Borchardt, *Gastroenterology*, 1989, **96**, 736–749.
77. P. Artursson and J. Karlsson, *Biochem Biophys Res Commun*, 1991, **175**, 880–885.
78. M.G.V. Pinto, M.R. Gómez, S. Seifert, B. Watzl, W.H. Holzapfel, C.M. Franz, *Int J Food Microbiol*, 2009, **133**, 86–93.
79. M. Eveillard, V. Fourel, M.C. Bare, S. Kernéis, M.H. Coconnier, T. Karjalainen, P. Bourlioux, A.L. Servin, *Mol Microbiol*, 1993, **7**, 371–381.
80. T. Zietek, E. Rath, D. Haller, H. Daniel, *Sci Rep*, 2015, **5**, 16831.
81. Y.G. Zhang, S. Wu, Y. Xia, J. Sun, *Physiol Rep*, 2014, **2**, e12147.
82. T. Sato, J.H. Van Es, H.J. Snippert, D.E. Stange, R.G. Vries, M. Van Den Born, N. Barker, N.F. Shroyer, M. Van De Wetering, H. Clevers, *Nature*, 2011, **469**, 415–418.

83. W. Lu, E. Rettenmeier, M. Paszek, M.F. Yueh, R.F. Tukey, J. Trottier, O. Barbier, S. Chen, *Drug Metab Dispos*, 2017, **45**, 748–754.
84. P. Jung, T. Sato, A. Merlos-Suárez, F.M. Barriga, M. Iglesias, D. Rossell, H. Auer, M. Gallardo, M.A. Blasco, E. Sancho, *Nat Med*, 2011, **17**, 1225–1227.
85. V. Rozehnal, D. Nakai, U. Hoepner, T. Fischer, E. Kamiyama, M. Takahashi, S. Yasuda, J. Mueller, *European Journal of Pharmaceutical Sciences*, 2012, **46**, 367–373.
86. K. Madsen, A. Cornish, P. Soper, C. McKaigney, H. Jijon, C. Yachimec, J. Doyle, L. Jewell, C. De Simone, *Gastroenterology*, 2001, **121**, 580–591.
87. P. Smith, C. Mirabelli, J. Fondacaro, F. Ryan, J. Dent, *Pharm Res*, 1988, **5**, 598–603
88. Å. Sjöberg, M. Lutz, C. Tannergren, C. Wingolf, A. Borde, A.L. Ungell, *Eur J Pharm Sci*, 2013, **48**, 166–180.
89. K. Worton, D. Candy, T. Wallis, G. Clarke, M. Osborne, S. Haddon, J. Stephen, *J Med Microbiol*, 1989, **29**, 283–294.
90. Y. Wang, D.B. Gunasekara, M.I. Reed, M. DiSalvo, S.J. Bultman, C.E. Sims, S.T. Magness, N.L. Allbritton, *Biomaterials*, 2017, **128**, 44–55.
91. D. Gao, H. Liu, J.M. Lin, Y. Wang, Y. Jiang, *Lab Chip*, 2013, **13**, 978–985.
92. M.B. Esch, G.J. Mahler, T. Stokol, M.L. Shuler, *Lab Chip*, 2014, **14**, 3081–3092.
93. K.Y. Shim, D. Lee, J. Han, N.T. Nguyen, S. Park, J.H. Sung, *Biomed Microdevices*, 2017, **19**.
94. P. Shah, J. V. Fritz, E. Glaab, M. S. Desai, K. Greenhalgh, A. Frachet, M. Niegowska, M. Estes, C. Jäger, C. Seguin-Devaux, F. Zenhausern and P. Wilmes, *Nat. Commun.*, 2016, **7**.
95. H. J. Kim, H. Li, J. J. Collins and D. E. Ingber, *Proc. Natl. Acad. Sci. U. S. A.*, 2016, **113**, E7–E15.
96. H. J. Kim and D. E. Ingber, *Integr. Biol.*, 2013, **5**, 1130–1140.

CHAPTER 2. A MICROFLUIDIC ORGANOTYPIC DEVICE FOR CULTURE OF MAMALLIAN INTESTINE EX VIVO

2.1 Summary

The physiological characteristics of the gastrointestinal (GI) tract are diverse and include rapid rates of epithelial turnover, complex nervous and immune systems, a thick mucus layer, and a large microbial population. Most GI models *in vitro* rely upon cell lines or organoids and consequently lack the diversity of cells and microorganisms present *in vivo*. *In vivo* studies retain function and cellular diversity but are more difficult to control. Microfluidic tissue-on-a-chip devices provide powerful alternatives for modeling physiological systems. Such devices show promise for use in GI research; however, most models use non-physiologic culture environments with higher than *in vivo* oxygen levels and insufficient gut microbiota. Our goal is to create a bridge between *in vitro* and *in vivo* using microfluidic devices by incorporating *ex vivo* tissue explants in physiologically relevant environments. Here, we report a microfluidic organotypic device (MOD) that enables media flow with differential oxygen concentrations across luminal and muscular surfaces of gut tissue *ex vivo*. Tissue was shown to be viable for 72 h and lowering oxygen concentration to a more physiologic level impacted bacterial populations.

2.2 Introduction

Intestinal tissue is composed of a complex network of epithelial, neural, immune, muscular, and vascular components.¹ Bacteria that inhabit the intestinal lumen are major contributors to maintaining intestinal homeostasis. An imbalance in microbial communities (dysbiosis) is associated with a variety of local tissue diseases such as inflammatory bowel (IBD) and celiac disease.^{2,3} More globally, dysbiosis influences disorders ranging from cardiovascular disease to

brain function.^{4,5} For *in vitro* and *ex vivo* intestinal models, cellular diversity and recapitulation of the *in vivo* environment is paramount to better understanding the relationship between dysbiosis and disease. For instance, bacterial cell products can activate intestinal neurons, leading to the release of inflammatory cytokines associated with IBD.⁶ Traditional *in vitro* cell culture can recapitulate some aspects of intestinal physiology and is useful for high throughput screening, but these models often rely upon cell monolayers to represent the intestinal barrier. Cell monolayers lack the *in vivo* cellular diversity from both a mammalian host and bacterial perspective and do not accurately represent the three-dimensional architecture of the intestinal wall.^{7,8} Three-dimensional intestinal organoids overcome some of these limitations by integrating multiple epithelial cell subtypes and exhibiting villus/crypt organization, but they are generally missing the neural, immune, and muscular components of the gut wall.^{8,9}

Improving upon static transwell models, ‘gut-on-a-chip’ microfluidic devices have been developed that allow media to be continuously perfused across opposing sides of a cell-seeded porous membrane representing the intestinal epithelial barrier.¹⁰⁻¹³ The incorporation of microfluidics in these devices improves cellular viability and longevity, constantly removes toxic cellular waste, and allows for controlled nutrient delivery.¹⁴ Recently, microbes have been incorporated into some *in vitro* microfluidic intestinal models by generating an oxygen gradient between microfluidic channels.¹⁵⁻¹⁹

Organotypic intestinal culture models are an attractive middle ground between *in vitro* and *in vivo* systems because they include the three-dimensional architecture of the gut wall while still providing easily controllable experimental parameters.²⁰ *Ex vivo* models of various tissues have been successfully used in microfluidic devices previously.²¹⁻²⁵ *Ex vivo* models, however, are generally low-throughput compared to cell-monolayer cultures and many have limited long-term

tissue viability.^{8,26} The Ussing chamber is a well-established *ex vivo* model for studying trans-epithelial drug, nutrient, and ion transport. While the Ussing chamber is valuable for pharmacokinetic/pharmacodynamic studies, viable epithelial tissue can only be maintained for several hours,^{27,28} making these models inappropriate for long-term host tissue-microbiome interaction studies.²⁹ In this report, we describe the design and testing of a microfluidic organotypic device (MOD) for use with mammalian intestinal explants *ex vivo*. The MOD houses full-thickness mouse intestinal tissue, including muscular, neural, immune, and epithelial components. The MOD system was used to maintain mouse intestinal explants for 72 h, with differential bacterial growth as a function of oxygen concentration.

2.3 Methods

Device prototypes were designed in SolidWorks (Dassault Systemes, Waltham, MA) and 3D printed with a Form 2 SLA printer (Formlabs, Somerville, MA). Once a final device design was established, the MOD was manufactured via injection molding (Applied Medical, Rancho Santa Margarita, CA) using cyclic olefin copolymer (COC; TOPAS Grade 8007) as material. All devices used during tissue testing were injection molded. Injection molding was chosen over other microfluidic device manufacturing methods because of its reproducibility and potential for large-scale manufacturing.³⁰ COC was chosen because of its biocompatibility, high chemical resistance, low oxygen permeability, and excellent optical properties.³¹⁻³³

The MOD (Figure 2.1) consists of three COC layers separated by polyurethane gaskets (PORON® AquaPro™, Rogers Corporation, Chandler, AZ); the gaskets define independent fluidic channels (10 mm wide, 1.1 mm deep, ~ 50 mm long, ~ 450 μ L). Intestinal tissue is housed in the middle layer such that the mucosa and serosa face independent channels. The edge of the tissue is supported by a thin lip molded into the middle layer, eliminating the need for a porous

membrane. The top layer was designed with integrated snap-fit fasteners for rapid, reversible assembly (Video S1), which is crucial to minimizing the time tissue explants are without media. Unlike other fasteners, snap-fit fasteners can be injection molded and enable consistent assembly regardless of the user. Both the top and bottom layers contain threaded inlet and outlet ports that connect to 10-32 PEEK finger-tight fittings (IDEX Health & Science, LLC, Oak Harbor, WA). Rubber O-rings were installed at the base of each port to ensure airtight leakproof connections

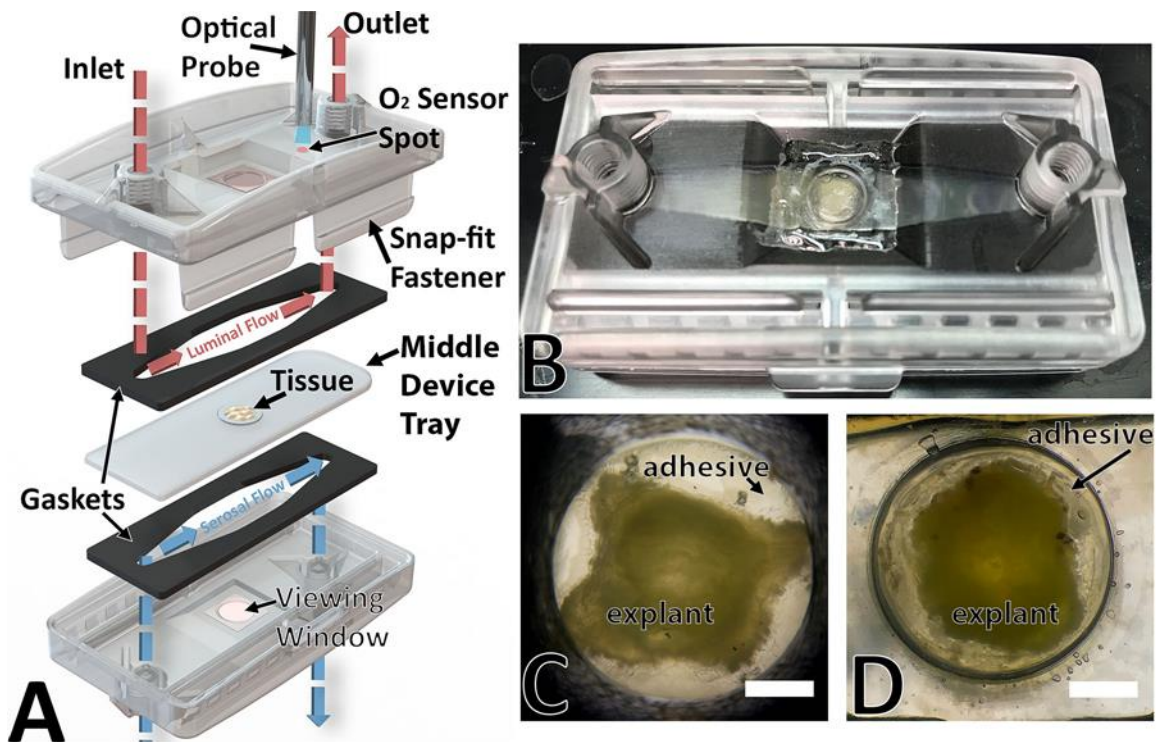


Figure 2.1 Schematic illustration of the MOD design and maintenance of tissue explants ex vivo. (A) an exploded model of the MOD system showing luminal (red) and serosal (blue) flow paths. (B) image of mouse colon explant inside the MOD. (C) image of colon explant tissue at 0h ex vivo through the viewing window. (D) image of different colon explant tissue at 72 h ex vivo through viewing window. Scale bars in C and D are 2 mm.

(IDEX Health & Science, LLC, Oak Harbor, WA). Glass coverslips (VWR, Radnor, PA) were fixed on the top and bottom layers using cyanoacrylate glue (Krazy Glue, Elmers Products, High Point, NC) directly above the tissue to enable on-chip imaging and tissue visualization (VWR, Radnor, PA). Quick setting epoxy was applied around the edges of the coverslips to further prevent

leakage and the top and bottom layers were placed in a 65° C oven for 15 min.

As a first step in instrumenting the device, oxygen sensor spots (OptiEnz, Fort Collins, CO) were adhered to the inner surface of the top layer downstream of the tissue chamber. The sensor's response was measured at two dissolved oxygen concentrations (DOC) using an external fiber optic probe (OptiEnz, Fort Collins, CO) to allow for the estimation of real-time DOC using the Stern-Volmer relationship:

$$\frac{\tau_0}{\tau} = 1 + K_{SV}[O_2] \quad , \quad (1)$$

where τ_0 is the luminescent decay time in the absence of oxygen, τ is the luminescent decay time in the presence of oxygen, K_{SV} is the Stern-Volmer constant, and $[O_2]$ is the oxygen concentration. Fluorescence of an oxygen-sensitive compound on the sensor spot is quenched in the presence of oxygen, leading to a reduction in luminescent decay time.³⁴

After assembly, each device was tested for failure modes, sterilized, and placed in a sterile environment until use. All fittings, ferrules, and tubing were submerged in diluted (1:10) bleach for 10 min, rinsed thoroughly with DI water, placed in a soapy water bath and vigorously scrubbed. After a second DI water rinse, the components and devices were submerged in a 70% ethanol solution containing 0.1% benzalkonium chloride for 30 min and rinsed with sterile water. Lastly, all other components including the gaskets and collection tubes were autoclaved at 120°C for 25 min. The devices could not be autoclaved due to COC's glass transition temperature of 78°C. Culture media was composed of CTS Neurobasal-A Medium (Thermo Fisher Scientific, Waltham, MA), 5% (v/v) 1M HEPES Buffer (Sigma Aldrich, St. Louis, MO), 2% (v/v) B-27 Supplement (Thermo Fisher Scientific, Waltham, WA) and supplemented with 10 μ M Nicardipine (Sigma Aldrich, St. Louis, MO), an L-type calcium ion channel blocker, that has previously been shown to block intestinal contractions *ex vivo*, a necessity when culturing intestinal tissue slices beyond

48 h.³⁵ CTS Neurobasal-A Medium was chosen as its predecessor, neurobasal media, has proven reliable in maintaining healthy explant slices from both mouse³⁵ and human³⁶ intestines, among numerous other organs^{37, 38, 39}. For each device, two syringes were filled with media (one containing 99.3 μ M fluorescein), connected to NE-300 syringe pumps (New Era Pump Systems Inc., Farmingdale, NY) and equilibrated in a 37°C incubator prior to experiments to remove any air bubbles formed by the expansion of dissolved gasses in the media. Mouse tissue was prepared as previously described³⁵ from mice approved under the Colorado State University IACUC protocol 17-720(A). Briefly, adult mice were sacrificed and the entirety of the large intestine was removed and placed in 4° C 1X Krebs buffer (in mM: 126 NaCl, 2.5 KCl, 2.5 CaCl₂, 1.2 NaH₂PO₄, 1.2 MgCl₂). The cecum was removed and the colon was cut longitudinally along the mesenteric border to open the lumen and form a flat sheet of tissue. Only ascending, transverse, and descending colon were used for device experiments. Tissue was free-hand dissected to form slices with a diameter of ~5 mm and placed in the center of the middle device layer. Cyanoacrylate glue was applied around the perimeter of the tissue to fill gaps between the tissue and plastic. While cyanoacrylate glue has been reported to be cytotoxic,⁴⁰ we only observed higher than expected levels of cell death where the glue directly contacted the tissue. After securing the tissue in the middle device layer, the device was quickly assembled by stacking successive layers separated by the gaskets and snapping them together. The devices were placed in a 37° C incubator, connected to syringes, and purged with media at a flow rate of 2.5 mL/hr. Media containing fluorescein was perfused through the luminal channel while media without fluorescein was perfused through the serosal channel. Once effluent media reached the collection tubes, the flow rate was reduced to 250 μ L/hr for the remainder of the experiments to provide low shear stress across the tissue. Collection tubes were changed every 10 h and immediately stored at -80°C. Colon explants used

for mucus experiments were cultured for 48 h before the addition of an azido-modified galactosamine, Tetraacetylated N-Azidoacetylgalactosamine (GalNAz; 12.5 μ M; Fisher Scientific, Pittsburgh, PA). At the conclusion of experiments, tissue explants were removed from the devices and placed in media containing either Ethidium Homodimer III (EtHD; Biotium, Hayward, CA) at a concentration of 2.5 μ M to evaluate cell death, or a fluorophore-tagged alkyne, Dibenzocyclooctyne-Cy3 (DBCO-Cy3; 2 μ M; Sigma-Aldrich, St. Louis, MO). After 30 min of incubation with EtHD, or 15 min of incubation with DBCO-Cy3, tissue explants were washed three times with culture media and fixed in 4% formaldehyde for a minimum of 8 h. Fixed tissue was washed with, and stored in, cold 0.05 M PBS until further analysis. A total of 27 devices were used for experiments, 4 of which were discarded due to breakage of the cyanoacrylate barrier separating the fluidic channels.

Fixed explants were sectioned at 50 μ m thick on a vibrating microtome (VT1000s, Leica Microsystems, Wetzlar, Germany) before mounting on glass microscope slides. Imaging was performed on a Nikon TE2000-U inverted microscope (20x Plan-Apo objective) with a UniBlitz shutter system (Vincent Associates, Rochester, NY) and an Orca-flash 4.0 LT camera (Hamamatsu, Hamamatsu City, Shizuoka Prefecture, Japan).

Fluorescein quantities contained in culture media effluents were analyzed using an Epoch Gen5 Microplate Spectrophotometer (BioTek, Winooski, VT) with a wavelength of 488 nm. Absorbance was quantified in effluent media from both channels in 10 h increments, with hour 0 representing initial placement of explants into devices. Background signal from phenol red, a component of CTS Neurobasal Medium, was removed.

2.4 Results and Discussion

Mouse colon explants were cultured in the MOD for up to 72 h *ex vivo* in both low and ambient mucosal DOC maintaining healthy, intact tissue (Supplemental Figure 1A-C). Tissue health was marked by maintenance of patterned rows of colonic crypts, with interspersed lamina propria and stereotypic arrangement of intestinal submucosal and muscular layers (Figure 2.2A, B, C). Minimal cell death was shown across 0h – 72h *ex vivo* (Figure 2.2D, E, F), indicated by labelling with EtHD. As expected, some EtHD was observed at the apical most epithelium, but not at the base of colonic crypts. Stem/progenitor cells at the base of colonic crypts proliferate and progeny migrate along the length of the crypt, towards the luminal aspect, before undergoing apoptosis and sloughing off into the intestinal lumen.⁴¹ This cycle is continuously repeated to regenerate a new epithelium every 2-3 days in the mouse.⁴² Minimal cell death observed throughout our explants during *ex vivo* culture, coupled with the EtHD signal at the apical most aspect of the crypt, points towards healthy tissue undergoing normal epithelial turnover. While others have maintained mammalian intestines in microfluidic devices for up to 72 h,⁴³ evidence of tissue health was minimal. Another concern in many systems^{15, 43-45} is that serum-containing media with supplemented antibiotics was used to culture the tissue. A key advantage of the MOD is that we have maintained tissue in serum-free media, without antibiotics, which enables controlled substance delivery to the tissue as well as studying the role of bacteria on tissue health and physiology.

In addition to maintaining viable tissue for 72 h, media was separated in independent microfluidic channels facing the mucosal and serosal sides of the tissue. Mean (+/- standard deviation) absorbance across all time points for luminal effluents was 0.11 +/- 0.03 and 0.00 +/-

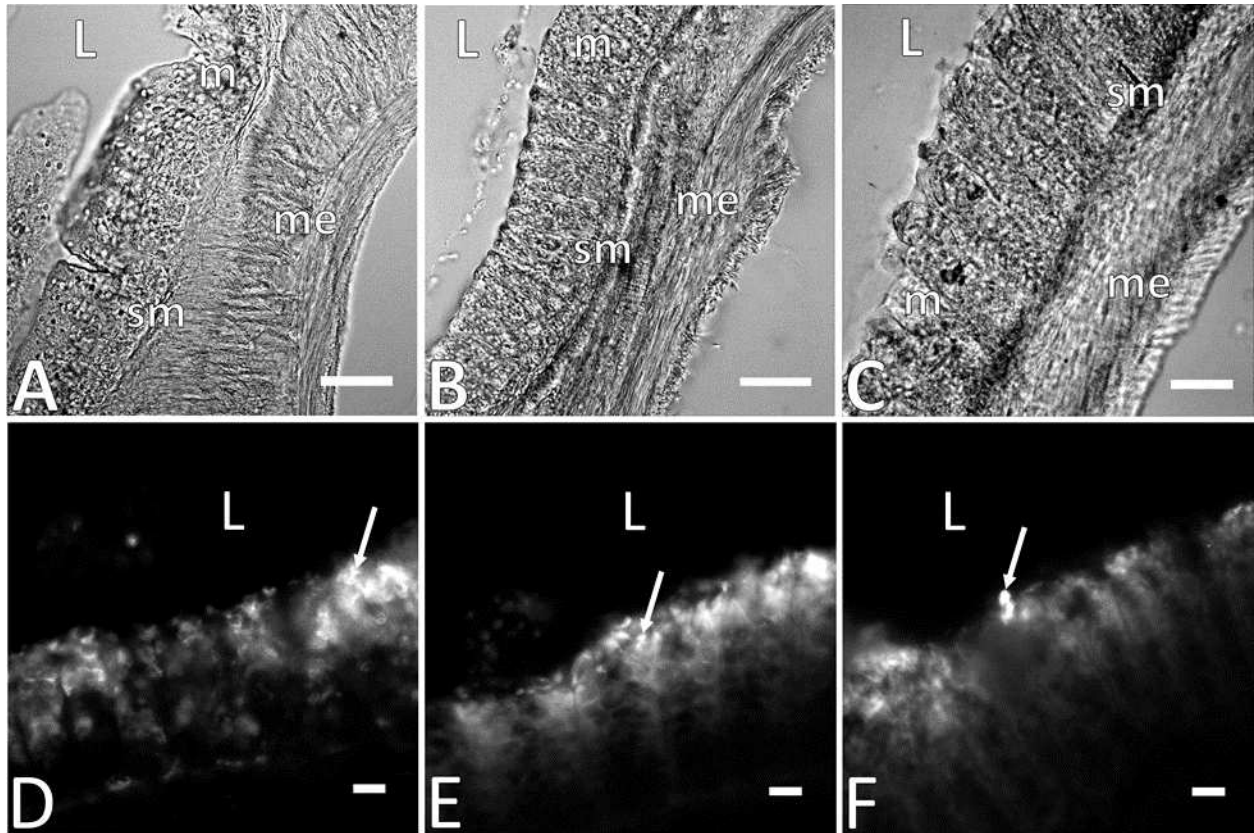


Figure 2.2 Tissue health was maintained for 72 h ex vivo in the MOD in both ambient and low oxygen conditions. Brightfield images in A-C demonstrate patterned rows of colonic crypts, and stereotypic anatomical arrangement of gut wall musculature and submucosa at 0h (A), 72 h in ambient oxygen (B) and 72 h in low oxygen (C). Fluorescent images in D-F demonstrate EtHD labelling in colonic explants, with stereotypic signal observed at apical most aspect of colonic crypts (arrows) at 0h (D), 72 h in ambient oxygen (E) and 72h in low oxygen (F). ‘L’ denotes intestinal lumen, ‘m’ indicates mucosa, ‘sm’ submucosa, and ‘me’ muscularis externa. Scale bars in A and B are 100 μm , scale bar in C is 50 μm , and scale bars in D-F are 25 μm .

0.02 for serosal effluents, indicating that media did not cross channels throughout the duration of the experiments (Figure 2.3). One potential concern is that fluorescein leakage could be diluted by the fluid flow, under the spectrophotometer’s detection limit. Since fluorescein and fluorescein-isothiocyanate are commonly used to assess barrier permeability in vivo⁴⁶ and in vitro,⁴⁷ any leakage below the detection limit is not biologically significant as an indication of barrier disruption. If media had crossed through the tissue, absorbance values would have increased substantially in the serosal effluent due to transfer or leakage of fluorescein across the tissue.

Another potential concern is the reliability of the cyanoacrylate seal around the tissue. In ~15% of the devices tested, tissue lost adhesion to the cyanoacrylate glue and media was allowed to freely transfer between channels. Future iterations of the MOD will be designed to reduce device failure rates and increase experimental repeatability. The verification of media separation is a critical indicator that the gut wall tissue retained one of its most essential features *ex vivo*, that of a physical barrier with tight junctions between cells. This helps ensure that pathogens, pharmaceuticals, and other compounds of interest for study *ex vivo* can only access tissue physiology by going through normal cellular processes (e.g., active transport, diffusion, cellular transfer). By comparison, in most organ-on-a-chip devices, a barrier is formed by a confluent cell monolayer without the underlying cellular diversity needed to understand intestinal physiology.

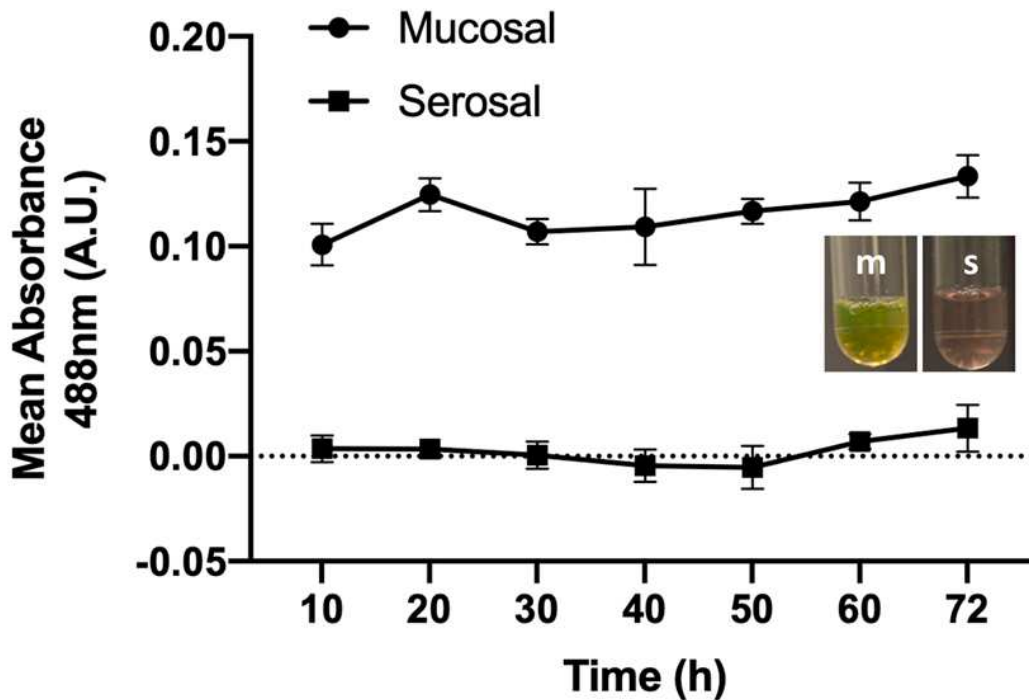


Figure 2.3 Media was separated across channels as marked by fluorescein absorbance in effluent media. Mean absorbance (A.U.) at 488 nm wavelength demonstrates significantly more fluorescein presence in mucosal (circular points) effluents compared to serosal (square points) ($P < 0.001$). No significant differences were observed across time in either the mucosal ($P > 0.20$) or serosal ($P > 0.45$) effluents. All statistical analyses were performed using a one-way ANOVA with $\alpha = .05$. Representative images show visible green color from fluorescein in mucosal (m) effluent compared to serosal (s) effluent.

The MOD enabled recapitulation of the *in vivo* oxygen gradient across the epithelial layer. DOC in the luminal channel were maintained at 3.0 +/- 0.38 mmHg for 48 h using 0.5 M sodium sulfite. *In vivo* intraluminal oxygen concentrations at the mucosal interface are nearly anoxic.⁴⁸ Perfusion of low oxygen-containing media within the luminal microfluidic channel increased bacterial presence on the tissue's mucosal surface compared to tissue perfused with media at ambient oxygen levels (~ 100 mmHg), as marked by fluorescent gram stain³⁵ (Figure 2.4A-F). Increases were most notable for gram-negative bacteria. Increased bacterial presence in a low oxygen environment was expected since many bacteria in the colon are anaerobic.⁴⁹ Therefore, recapitulation of the *in vivo* oxygen gradient is vital to studying host tissue interactions with a more diverse, physiologically relevant bacterial community. It is also important to note that these experiments are proof-of-principle. Quantifying specific bacteria and overall bacteria concentrations will be the focus of future reports.

Microfluidics provide a mechanism of tissue perfusion *ex vivo* that should allow for healthier tissue over longer periods.¹⁴ Previous *ex vivo* systems such as intestinal organotypic slices maintained tissue for 6 days, but without a true luminal barrier.³⁵ Other methods such as Ussing chambers maintain full thickness tissues with an intact barrier, but with limited viability over a few hours.²⁷ Using dual flow microfluidics, the MOD allows for the culture of full thickness explants with an intact barrier over an extended length of culture (3 days).

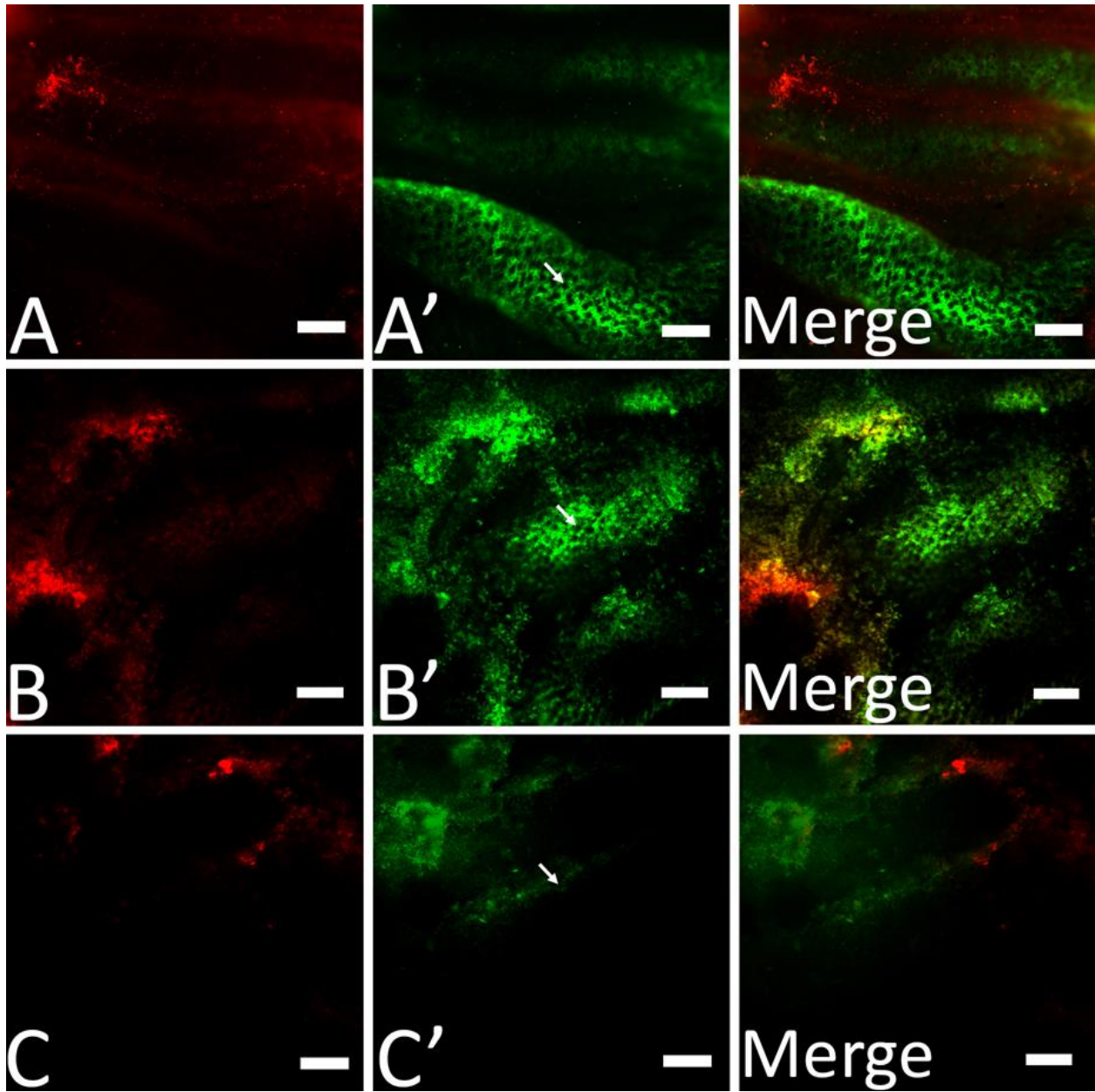


Figure 2.4 Microbiota were maintained in the MOD, and more bacteria were visible in an explant cultured in lower oxygen conditions. Baseline bacterial levels are shown at 0h ex vivo via hexidium iodide ($7.05 \mu\text{M}$) fluorescence in red (A), signifying Gram-positive bacteria, and SYTO9 ($5.01 \mu\text{M}$) fluorescence in green (A'), signifying Gram-negative bacteria. Gram stain fluorescence was noticeably higher in tissue cultured in lowered oxygen conditions (B-B'; 3 mmHg) when compared to tissue cultured in ambient oxygen (C-C'; 100 mmHg) containing media. Arrows in A', B' and C' denote a single colonic crypt. Scale bars in all panels are $100 \mu\text{m}$.

2.5 Conclusion

In conclusion, a novel *ex vivo* microfluidic organotypic device was designed and tested. This system maintains viable polarized murine intestinal explants for 72 h *ex vivo* and enables a physiological oxygen gradient to be established between independent microfluidic channels rendering luminal and vascular compartments. The MOD bridges a substantial gap in current approaches to modeling barrier tissue as it overcomes several limitations associated with both *in vitro* and *in vivo* models. Due to the culture of full thickness explants, the MOD more closely recapitulates the *in vivo* physiology of the gut wall, as tissue explants include the complex cellular diversity and native tissue structural relationships of the gut wall. The MOD system offers a novel approach to culturing intestinal tissues with intact luminal barriers.

Future extensions to the MOD will include developing and integrating optical and/or electrochemical sensors for analytes relevant to the intestinal environment (i.e. glucose, lactate). Electrodes can be added to assess transepithelial electrical resistance, which has been a useful measure of barrier integrity in other systems.^{15,50,51} Ultimately, the MOD will be implemented in long-term microbiome studies to elucidate the relationship among microbial, epithelial, neuro and immune components of the gut wall in health and disease.

REFERENCES

1. J. M. Wells, O. Rossi, M. Meijerink and P. van Baarlen, *Proc. Natl. Acad. Sci.*, 2010, **108**, 4607–4614.
2. S. Ghaisas, J. Maher and A. Kanthasamy, *Pharmacol. Ther.*, 2016, **158**, 52–62.
3. S. Carding, K. Verbeke, D. Vipond, B. Corfe and L. Owen, *Microb. Ecol. Heal. Dis.*, 2015, **26**, 26191.
4. A. B. Shreiner, J. Y. Kao and V. B. Young, *Curr Opin Gastroenterol*, 2015, **31**, 69–75.
5. H. Jiang, Z. Ling, Y. Zhang, H. Mao, Z. Ma, Y. Yin, W. Wang, W. Tang, Z. Tan, J. Shi, L. Li and B. Ruan, *Brain. Behav. Immun.*, 2015, **48**, 186–194.
6. C. Bernardazzi, B. Pêgo and H. S. P. De Souza, *Mediators Inflamm.*, 2016, DOI:10.1155/2016/1363818.
7. T. Lea, in *The Impact of Food Bioactives on Health*, 2015, pp. 103–111.
8. A. Bein, W. Shin, S. Jalili-firoozinezhad, M. H. Park, A. Sontheimer-phelps, A. Tovaglieri, A. Chalkiadaki, H. J. Kim and D. E. Ingber, *Cell. Mol. Gastroenterol. Hepatol.*, 2018, **5**, 659–668.
9. L. A. Schwerdtfeger and S. A. Tobet, *J. Neuroendocrinol.*, 2018, e12650.
10. H. J. Kim and D. E. Ingber, *Integr. Biol.*, 2013, **5**, 1130.
11. K. Y. Shim, D. Lee, J. Han, N. T. Nguyen, S. Park and J. H. Sung, *Biomed. Microdevices*, 2017, **19**, 37.
12. W. Shin and H. J. Kim, *Proc. Natl. Acad. Sci.*, 2018, **115**, E10539–E10547.
13. M. B. Esch, J. H. Sung, J. Yang, C. Yu, J. Yu, J. C. March and M. L. Shuler, *Biomed. Microdevices*, 2012, **14**, 895–906.
14. I. C. Mclean, L. A. Schwerdtfeger, S. A. Tobet and C. S. Henry, *Lab Chip*, 2018, **18**, 1399–1410.
15. P. Shah, J. V. Fritz, E. Glaab, M. S. Desai, K. Greenhalgh, A. Frachet, M. Niegowska, M. Estes, C. Jäger, C. Seguin-Devaux, F. Zenhausern and P. Wilmes, *Nat. Commun.*, 2016, 7:11535, DOI:10.1038/ncomms11535.
16. M. Marzorati, B. Vanhoecke, T. De Ryck, M. S. Sadabad, I. Pinheiro, S. Possemiers, P. Van Den Abbeele, L. Derycke, M. Bracke, J. Pieters, T. Hennebel, H. J. Harmsen, W. Verstraete and T. Van De Wiele, *BMC Microbiology*, 2014, **14**, 133.
17. H. J. Kim, H. Li, J. J. Collins and D. E. Ingber, *Proc. Natl. Acad. Sci.*, 2015, **113**, E7–E15.
18. W. Shin, A. Wu, M. W. Massidda, C. Foster, N. Thomas, D.-W. Lee, H. Koh, Y. Ju, J. Kim and H. J. Kim, *Front. Bioeng. Biotechnol.*, 2019, **7**, 1–13.
19. S. Jalili-Firoozinezhad, F. S. Gazzaniga, E. L. Calamari, D. M. Camacho, C. W. Fadel, A. Bein, B. Swenor, B. Nestor, M. J. Cronce, A. Tovaglieri, O. Levy, K. E. Gregory, D. T. Breault, J. M. S. Cabral, D. L. Kasper, R. Novak and D. E. Ingber, *Nat. Biomed. Eng.*, , DOI:10.1038/s41551-019-0397-0.

20. R. Nunes, C. Silva and L. Chaves, in *Concepts and Models for Drug Permeability Studies: Cell and Tissue Based in Vitro Culture Models*, 2016, pp. 203-236.
21. S. Xiao, J. R. Coppeta, H. B. Rogers, B. C. Isenberg, J. Zhu, S. A. Olalekan, K. E. McKinnon, D. Dokic, A. S. Rashedi, D. J. Haisenleder, S. S. Malpani, C. A. Arnold-Murray, K. Chen, M. Jiang, L. Bai, C. T. Nguyen, J. Zhang, M. M. Laronda, T. J. Hope, K. P. Maniar, M. E. Pavone, M. J. Avram, E. C. Sefton, S. Getsios, J. E. Burdette, J. J. Kim, J. T. Borenstein and T. K. Woodruff, *Nat. Commun.*, 2017, 8, 14584.
22. A. E. Ross, M. C. Belanger, J. F. Woodroof and R. R. Pompano, *Analyst*, 2017, 142, 649.
23. K. H. Dodson, F. D. Echevarria, D. Li, R. M. Sappington and J. F. Edd, *Biomed. Microdevices*, 2015, 17, 114.
24. B. Atac, I. Wagner, R. Horland, R. Lauster, U. Marx, A. G. Tonevitsky, R. P. Azar and G. Lindner, *Lab Chip*, 2013, 13, 3555–3561.
25. S. Yasotharan, S. Pinto, J. G. Sled, S.-S. Bolz and A. Günther, *Lab Chip*, 2015, 15, 2660–2669.
26. S. C. Pearce, H. G. Coia, J. P. Karl, I. G. Pantoja-Feliciano, N. C. Zachos and K. Racicot, *Front Physiol.*, 2018, 9, 1584
27. L. L. Clarke, *Am J Physiol Gastrointest Liver Physiol.*, 2009, 296, 1151–1166.
28. B. Kisser, E. Mangelsen, C. Wingolf, L. I. Partecke, C. Heidecke, C. Tannergren, S. Oswald and M. Keiser, *Curr Protoc Pharmacol.*, 2017, 77, 1–19.
29. S. May, S. Evans and L. Parry, *Emerg. Top. Life Sci.*, 2017, 1, 385–400.
30. G. S. Fiorini and D. T. Chiu, *Biotechniques*, 2005, 38, 429–446.
31. M. Berenguel-alonso, M. Sabés-alsina, R. Morató, O. Ymbern, L. Rodríguez-vázquez, O. Talló-parra, J. Alonso-chamarro, M. Puyol and M. López-béjar, *SLAS Technol.*, 2017, 22, 507–517.
32. P. M. Van Midwoud, A. Janse, M. T. Merema, G. M. M. Groothuis and E. Verpoorte, *Anal. Chem.*, 2012, 84, 3938–3944.
33. C. J. Ochs, J. Kasuya, A. Pavesi and R. D. Kamm, *Lab Chip*, 2014, 14, 459–462.
34. X. D. Wang and O. S. Wolfbeis, *Chem. Soc. Rev.*, 2014, 43, 3666–3761.
35. L. A. Schwerdtfeger, E. P. Ryan and S. A. Tobet, *Am J Physiol Gastrointest Liver Physiol*, 2016, 310, 240–248.
36. L. A. Schwerdtfeger, N. J. Nealon, E. P. Ryan and S. A. Tobet, *PloS one*, 2019, 14, e0217170.
37. E. P. Bless, H. J. Walker, K. W. Yu, J. G. Knoll, S. M. Moenter, G. A. Schwarting and S. A. Tobet, *Endocrinology*, 2005, 146, 463-468.
38. A. M. Navratil, J. G. Knoll, J. D. Whitesell, S. A. Tobet and C. M. Clay, *Endocrinology*, 2007, 148, 1736-1744.
39. W. Tedjo, J. E. Nejad, R. Feeny, L. Yang, C. S. Henry, S. Tobet and T. Chen, *Biosens Bioelectron*, 2018, 114, 78-88.

40. P. A. Leggat, U. Kedjarune and D. R. Smith, *Ind. Health*, 2004, **42**, 207–211.
41. J. M. Allaire, S. M. Crowley, H. T. Law, S. Y. Chang, H. J. Ko and B. A. Vallance, *Trends Immunol.*, 2018, **39**, 677–696.
42. H. Chong and M. Bjerknes, [Anat Rec.](#), 1983, **207**, 423-434
43. A. Dawson, C. Dyer, J. Macfie, J. Davies, L. Karsai, J. Greenman and M. Jacobsen, *Biomicrofluidics*, 2016, **10**, DOI:10.1063/1.4964813.
44. S. Oh, H. Ryu, D. Tahk, J. Ko, Y. Chung, H. K. Lee, T. R. Lee and N. L. Jeon, *Lab Chip*, 2017, **17**, 3405–3414.
45. M. Astolfi, F. Saad, F. Monet, E. Carmona, B. Péant, M. A. Lateef, J. Kendall-Dupont, A.-M. Mes-Masson, N. Rousset, T. Gervais and D. Provencher, *Lab Chip*, 2016, **16**, 312–325.
46. E. A. Vicuna, V.A. Kuttappan, R. Galarza-Seeber, J.D. Latorre, O.B. Faulkner, B.M. Hargis, G. Tellez, L. R. Bielke, *Poultry Science*, 2015, 94, 2075-2080.
47. L. Zhang, J. Song, T. Bai, W. Qian, X. Hou, *Scientific Reports*, 2017, 7, 4950.
48. L. Albenburg, T. V. Esipova, C. Judge, K. Bittinger, J. Chen, A. Laughlin, S. Grunberg, R. N. Baldassano, J. D. Lewis, H. Li, S. R. Thom, F. D. Bushman, S. A. Vinogradov and G. Wu, *Gastroenterology*, 2014, **147**, 1055–1063.
49. W. Shin, A. Wu, M. W. Massidda, C. Foster, N. Thomas, D.-W. Lee, H. Koh, Y. Ju, J. Kim and H. J. Kim, *Front. Bioeng. Biotechnol.*, 2019, **7**, 1–13.
50. O. Y. F. Henry, R. Villenave, M. J. Counce, W. D. Leineweber, M. A. Benz and D. E. Ingber, *Lab Chip*, 2017, **17**, 2264–2271.
51. J. J. Srinivasan, B.; Kolli, A.R.; Esch, M.B.; Abaci, H.E.; Shuler, L.; Hickman, B. Srinivasan, A. R. Kolli, M. B. Esch, H. E. Abaci, M. L. Shuler and J. J. Hickman, [J Lab Autom.](#), 2015, **20**, 107-126

*** This chapter is reproduced from the following reference:**

A. Richardson, L. A. Schwerdtfeger, D. Eaton, I. McLean, C. S. Henry and S. A. Tobet, *Anal. Methods*, 2020, **12**, 297–303.

CHAPTER 3: A MAGNETICALLY ASSEMBLED MICROFLUIDIC SENSOR MODULE FOR ORGAN-ON-A-CHIP SYSTEMS

3.1 Introduction

As Organ-on-a-Chip (OOC) technologies continue to evolve, there is a growing need for integrated sensors that enable real-time monitoring of tissue-specific physiological processes. Traditional analytical methods heavily rely on sample collection and off-chip assays which lack sufficient temporal resolution and require large working volumes.¹ Two classes of sensors, electrochemical and optical, are well suited for integration into OOC devices because they are highly sensitive and selective, cost-effective, can be readily fabricated at micro scales, and exhibit fast response times.² Indeed, numerous OOC devices feature on-chip electrochemical or optical biosensors to monitor changes in environmental parameters (e.g. O₂, pH, CO₂),³⁻⁶ metabolic products (e.g. glucose, lactate),^{7,8} and cell-secreted molecules (e.g. cytokines)^{9,10} amongst other biomolecules. Due to limited on-chip space, a common approach is to integrate sensors into microfluidic platforms in-line with chips containing cells or tissues. Off-chip auxiliary sensor modules are particularly useful for multi-organ models and Body-on-a-Chip systems requiring simultaneous detection of many analytes in real-time. For example, Zhang et al. developed a liver/heart OOC platform with inline bioelectrochemical and physical/chemical sensing modules to monitor microenvironment parameters and measure soluble protein biomarkers in real-time. However, one drawback to this system and many others is that the sensors and microfluidic chips are irreversibly bound, requiring both components to be refabricated if either component fails. Alternatively, sensor modules designed with plug-and-play architectures are advantageous because individual sensors can be hot-swapped when failures occur, and microfluidic platforms can be reused in separate experiments requiring different sensors. Examples of plug-and-play

sensor modules include 3D-printed microfluidic devices that accommodate electrochemical sensors housed in PEEK finger-tight fittings¹¹ or custom holders,^{12,13} as well as a 3D-printed flow cells that accommodate off-the-shelf optical components.^{14,15}

3D-printing is an attractive method for microfluidic device fabrication because it enables rapid prototyping of different designs in one step, and in some cases, multiple materials with different mechanical properties can be printed simultaneously.^{13,16} One disadvantage to 3D-printing microfluidic devices is the need to remove uncured material from internal channels, which is challenging and time-consuming.¹⁷ Channel clogging can be circumvented by 3D-printing open-faced microfluidic devices and reversibly or irreversibly sealing the printed parts to various substrates.¹⁸⁻²¹ Reversibly sealed microfluidic devices are especially desirable for OOC applications because they can be disassembled, sterilized, and reused following experiments.²² Different methods have been used to reversibly seal microfluidic devices, such as adhesive bonds,^{23,24} vacuum suction,^{25,26} and mechanical clamps fastened with screws^{27,28} or magnets.²⁹⁻³³

Here, we report a novel plug-and-play sensor module for use in OOC systems. The microfluidic platform consists of two 3D-printed layers separated by either a silicone gasket or PDMS chip with defined microfluidic channels. Magnets installed in each 3D printed layer provide high-pressure reversible seals and allow for rapid assembly and disassembly. The top 3D-printed layer contains threaded ports that accommodate both electrochemical and optical sensors housed in commercial PEEK finger tight fittings. Importantly, this design reduces fabrication costs since both the microfluidic platform and sensors can be cleaned and reused between experiments. Additionally, the sensor module's plug-and-play architecture enables it to be used for different experiments and OOC systems.

3.2 Methods

Device Design

Devices were designed in SolidWorks CAD software (Dassault Systemes, Waltham, MA) and the top and bottom layers were 3D-printed with a Form 3 SLA printer (Formlabs, Somerville, MA) using Clear V4 resin. After printing, the devices were soaked in isopropyl alcohol for 20 minutes to remove uncured resin and subsequently post-cured according to Formlabs recommendations. All 3D-printed devices were coated with a silicone-modified conformal coating (MG Chemicals, Surrey, BC) to provide a smooth surface finish and improve optical transparency. N42 Neodymium bar magnets (K&J Magnets Inc., Pipersville, PA) were installed in slots on the inner surface of each 3D-printed layer using cyanoacrylate glue (Krazy Glue, Elmers Products, High Point, NC), providing ~11.5 lbf of total clamping force. Since the pull force between two magnets is reduced by a factor of 2 when separated by only 650 μm , the device was intentionally designed such that opposing magnets are nearly in contact after device assembly. Shown in Figure 3.1, we designed two distinct microfluidic platforms with different middle layers to demonstrate the versatility of magnetic connections.

In the first design (fig. 3.1A), the middle layer consists of a 20A durometer silicone gasket (McMaster-Carr, Elmhurst, IL) cut with an Epilog Zing laser cutter to define the microfluidic channel (1 mm width, 200 μm height, 33 mm length). To ensure a consistent channel height, the gasket was compressed by a set percent (25%) of its original thickness. The allowable percent compression was estimated by first converting the maximum clamping force provided by the magnets to a clamping pressure using the following equation:

$$P_{clamp} = \frac{F_{clamp}}{SA_{gasket}} \quad (1)$$

P_{clamp} was subsequently compared to a compression-deflection curve for 20A durometer silicone gaskets, which defines the pressure needed to compress a material by a given percent. The top 3D-printed layer contains threaded inlet/outlet ports and two sensor ports that are compatible with 10-32 and 1/4-28 finger-tight fittings (IDEX Health and Science, LLC, Oak Harbor, WA), respectively. The bottom 3D printed layer features notches aligned with the sensor ports which prevent installed sensors from occluding the microfluidic channel. Rubber O-rings were installed at the base of the inlet/outlet ports to ensure leak-free connections.

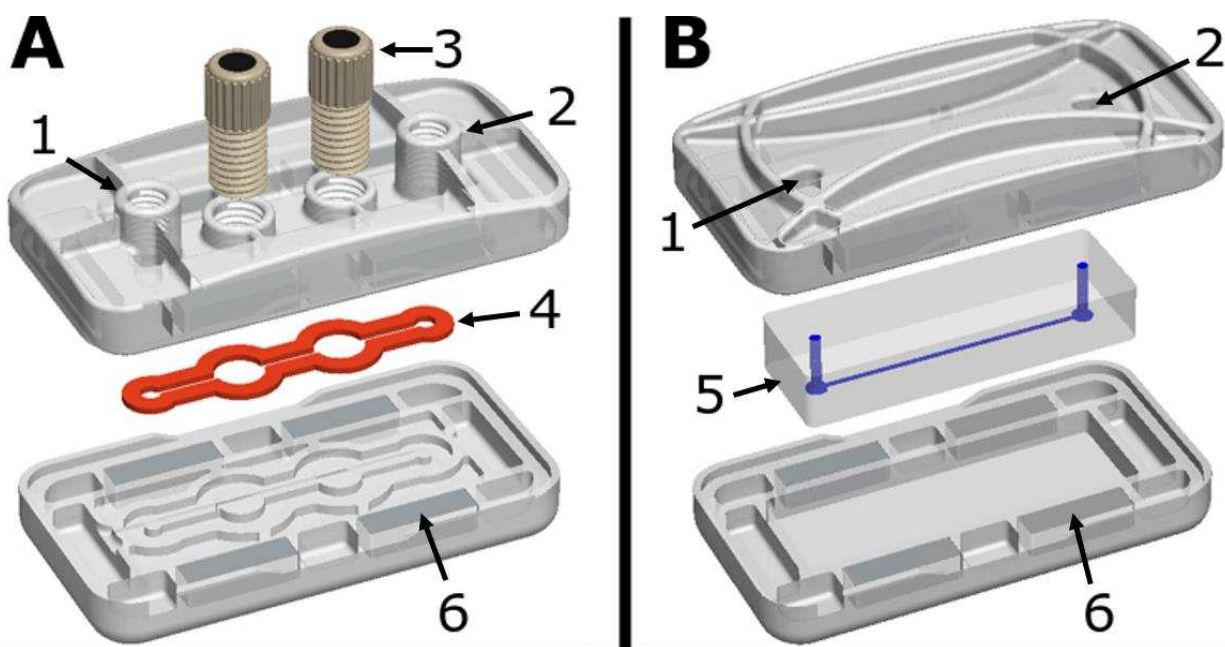


Figure 3.1 CAD drawing of the magnetically assembled sensor module. **A)** In design 1, the microfluidic channel is defined by a laser cut gasket. **B)** In design 2, the microfluidic channel is embedded in a PDMS chip. **1-6** indicate the fluid inlet, fluid outlet, electrochemical sensors, gasket, PDMS chip, and magnets, respectively.

In the second design (fig. 3.1b), the middle layer comprises a PDMS chip with an open-faced microfluidic channel (500 μm width, 200 μm height, 33 mm length). The PDMS chip was fabricated using a 3D-printed mold combined with conventional soft lithographic techniques (Qin 2010). Briefly, Sylgard 184 silicone elastomer base and Sylgard 184 elastomer curing agent were thoroughly mixed at a 10:1 ratio and degassed in a vacuum desiccator. The mixture was then cast

over the 3D-printed mold and cured for 24 h in an 80°C oven. A 10:1 elastomer base to curing agent ratio was chosen because higher ratios (e.g. 15:1) resulted in significant channel deformation under compression. 18G steel connectors were inserted into biopsy-punched holes at the inlet and outlet to establish fluidic connections.

Leakage Tests

We evaluated the sealing performance of each device design with two different magnet arrangements. Magnets were either installed along the devices' sides parallel to the channel axis or around the devices' periphery providing more equal spacing. Leakage tests were carried out as follows:

1. A 60 mL syringe filled with colored DI water was loaded on an NE-300 syringe pump (New Era Pump Systems Inc., Farmingdale, NY) and connected to an assembled device using commercial fittings and tubing.
2. An F-238 NanoTight Capillary sleeve (IDEX Health and Science, LLC, Oak Harbor, WA) was connected to the device's outlet to provide additional fluidic resistance.
3. Fluid was pumped through the device for 30 seconds in 0.5 mL/min increments until leakage was observed. This process was repeated for all devices and magnet arrangements.

Volumetric flow rates (Q) were converted to pressure values (ΔP) using the following equation:

$$\Delta P = QR_{total} \quad (2)$$

R_{total} is the combined fluidic resistance provided by the microfluidic channel and capillary sleeve. The individual resistance contributions from the microfluidic channel and capillary sleeve were calculated from equations 3 and 4, respectively:

$$R_{channel} = \frac{12\mu L}{wh^3\left(1-0.63\frac{h}{w}\right)} \quad (3)$$

$$R_{capillary} = \frac{8\mu L}{\pi r^4} \quad (4)$$

Here, μ is the dynamic viscosity, L is the channel length, w is the channel width, h is the channel height, and r is the capillary inner diameter.

Electrode Fabrication

Electrochemical sensors were made by heat-pressing a previously reported thermoplastic electrode (TPE) material³⁴ into ¼-28 PEEK finger-tight fittings. To fabricate the electrode material, polycaprolactone (PCL) pellets (ThermoMorph®) were first dissolved in dichloromethane followed by the addition of graphite (Grade 3569, Asbury Graphite Mills, INC., Asbury, NJ) at a 3:1 (w/w) graphite to PCL ratio. Once homogenized, the mixture was poured onto a silicon wafer and the solvent was allowed to evaporate. The dried material was then molded into finger-tight fittings using a hydraulic heat press set to 75°C. Next, the ends of the finger-tight fittings were sanded and polished to remove contaminants, and the electrodes' conductivity were measured for quality control purposes. Electrical connections were established using electrical wire and silver paint, and epoxy was applied over the connections for mechanical reinforcement. Prior to electrochemical experiments, finger-tight fittings were wrapped with Teflon tape to prevent leakage from the sensor ports.

Electrochemical Experiments

We characterized the electrodes' electrochemical performance via flow injection analysis coupled with amperometry. A 6-port valve actuator (Scivex, Oak Harbor, WA) was used for sample injection while a CHI832 bipotentiostat (CH Instruments, Inc., Austin, TX) was used for

electrochemical measurements. Two finger-tight fittings containing working electrodes were screwed into the sensor module's sensor ports such that the electrodes were flush with the microfluidic channel. A saturated calomel reference electrode and platinum counter electrode were placed in a downstream waste beaker filled with 0.1 M potassium chloride (KCl). Initially, 0.1 M KCl was pumped through the device to establish a baseline current. Then, a 10 μ L sample of 1 mM ferrocene-trimethylamine (FcTMA⁺) in 0.1 M KCl was injected into the device, causing a change in current due to the oxidation and reduction of FcTMA⁺ at different working electrodes. This step was repeated several times after reestablishing the baseline current.

3.3 Results and Discussion

The sensor module exhibited excellent sealing capabilities across all device designs/magnet arrangements and withstood backpressures as high as 322 kPa. Illustrated in Figure 3.2, the burst pressure was significantly higher for devices designed with a gasket material compared to devices designed with a PDMS chip. One potential explanation for the difference in burst pressure between the two designs is that the PDMS chip has nearly 4 times more surface area than the gasket (0.86 in² vs. 0.22 in²). While the magnets provide equal clamping force for both designs, the large surface area of the PDMS chip reduces the applied clamping pressure. Another potential explanation for the burst pressure difference is that the PDMS chip was cast in a 3D-printed mold, resulting in surface irregularities that could reduce sealing effectiveness. Regardless of the design, the sensor module withstood higher backpressures compared to most previously reported microfluidic devices reversibly sealed with magnetic connections. Tkachenko et al., Abhyankar et al., and Rasponi et al. reported magnetic clamping systems for cell culture applications with burst pressures as high as 40 kPa, 35 kPa, and 58 kPa, respectively. Rafat et al. and Occhetta et al. reported devices with even higher burst pressures (145 kPa, 150 kPa). However,




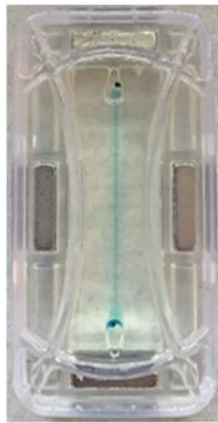
	<u>Gasket: 1</u>	<u>Gasket: 2</u>	<u>PDMS: 1</u>	<u>PDMS: 2</u>
Device: Magnet Arrangement				
Avg. Flow Rate (mL/min)	10.5	11.4	4	5.3
Avg. Burst Pressure (kPa)	297	322	118	156

Figure 3.2 Comparison of the average flow rates and corresponding burst pressures between different device designs and magnet arrangements. Burst pressures were significantly different between Gasket:1 and PDMS:1; Gasket:2 and PDMS:2 ($P < .01$) as well as between PDMS:1 and PDMS:2 ($P < .05$). Burst pressures were not significantly different between Gasket:1 and Gasket:2. $n=4$ for all device designs and magnet arrangements.

all these devices were designed to clamp PDMS chips alone, whereas the sensor module is capable of clamping multiple materials. In addition to comparing the sensor module's sealing effectiveness using different materials, we investigated whether different magnet arrangements provided more reliable seals. Higher burst pressures were seen in devices with magnets distributed equally around the perimeter (magnet arrangement 2), although the difference was not significant for gasketed devices. Magnet arrangement 2 provided more clamping force near the devices' inlets and outlets where leakages typically occurred. Overall, any of the tested designs/magnet arrangements are suitable for OOC applications because the flow rates in OOC devices are typically an order of magnitude lower than the flow rates we used for leakage tests.

To demonstrate that the sensor module can accommodate multiple electrochemical sensors simultaneously, we measured the oxidation and reduction of FcTMA^+ at different working

electrodes with shared downstream reference and counter electrodes (Figure 3.3). After injecting samples into the device, FcTMA⁺ was oxidized at the upstream working electrode (WE1) with a perturbation voltage of +400 mV. Then, FcTMA²⁺ was reduced at the downstream working electrode (WE2) with a perturbation voltage of +200 mV. This shows that the working electrodes function independently despite sharing the same counter and reference electrodes. The first sample injection resulted in peak oxidation and reduction currents of 5.2e-7 A and -2.0e-7 A, respectively. Subsequent sample injections resulted in consistent peak oxidation and reduction currents of 6.5 ± 0.1e-7 A and -2.4 ± 0.06e-7 A, respectively. To this point, we have only characterized FcTMA⁺ redox chemistry in the sensor module. However, our group has previously reported TPE's with covalent surface modifications,³⁵ thus opening the possibility to fabricate TPE-based biosensors that could be integrated into the sensor module.

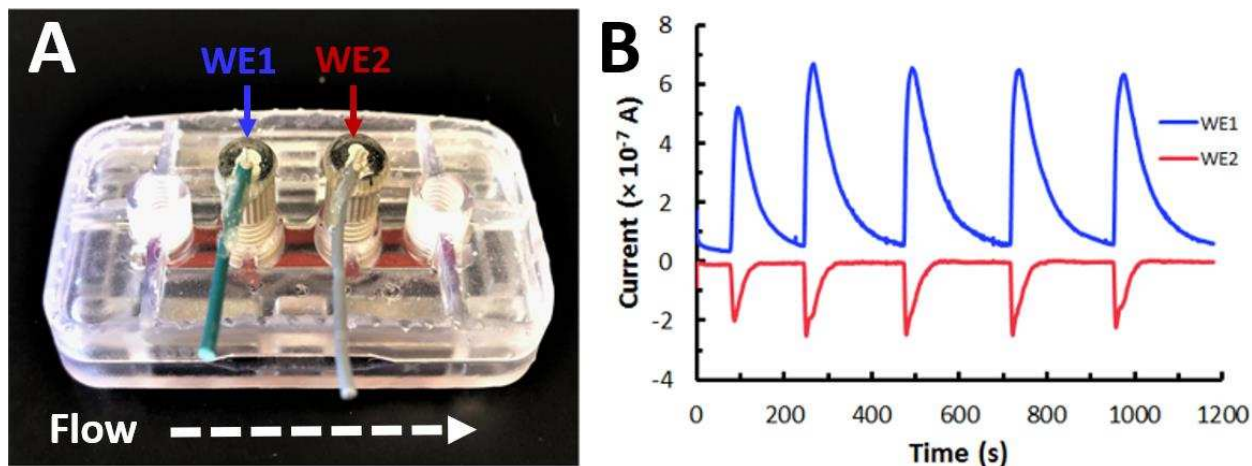


Figure 3.3 Electrochemical detection of ferrocene-trimethylamine (FcTMA⁺) redox chemistry. A) representative sensor module with two working electrodes in line with the microfluidic channel. B) Amperogram showing the repeated oxidation (blue peaks) and reduction (red peaks) of FcTMA⁺.

3.4 Conclusion

In conclusion, we designed and tested a microfluidic sensor module reversibly sealed with magnetic connections. The device could clamp both gaskets and PDMS chips with different magnet arrangements, enabling leak-free seals at high backpressures. Further, we integrated

reusable TPEs into commercial finger-tight fittings and detected the oxidation/reduction of FcTMA⁺ at different working electrodes in the sensor module. Optical sensors could be integrated into finger-tight fittings by fixing polymeric thin films containing analyte sensitive dyes to the bottom of the fittings. The fitting's hollow core would allow fiber optic probes to be easily aligned with the polymeric thin film. In the future, the sensor module will be implemented in OOC systems such as the previously reported microfluidic organotypic device (MOD)⁶ for real time sensing of analytes like glucose and lactate.

REFERENCES

1. Y. S. Zhang, J. Aleman, S. R. Shin, T. Kilic, D. Kim, S. A. M. Shaegh, S. Massa, R. Riahi, S. Chae, N. Hu, H. Avci, W. Zhang, A. Silvestri, A. S. Nezhad, A. Manbohi, F. De Ferrari, A. Polini, G. Calzone, N. Shaikh, P. Alerasool, E. Budina, J. Kang, N. Bhise, J. Ribas, A. Pourmand, A. Skardal, T. Shupe, C. E. Bishop, M. R. Dokmeci, A. Atala and A. Khademhosseini, *PNAS*, 2017, **114**, E2293–E2302.
2. K. Rajpoot, *Biosens. J.*, 2017, **6**, DOI:10.4172/2090-4967.1000145.
3. P. Shah, J. V. Fritz, E. Glaab, M. S. Desai, K. Greenhalgh, A. Frachet, M. Niegowska, M. Estes, C. Jäger, C. Seguin-Devaux, F. Zenhausern and P. Wilmes, *Nat. Commun.*, 2016, **7**, DOI:10.1038/ncomms11535.
4. M. H. Wu, J. L. Lin, J. Wang, Z. Cui and Z. Cui, *Biomed. Microdevices*, 2009, **11**, 265–273.
5. S. E. Eklund, D. E. Cliffel, E. Kozlov, A. Prokop, J. Wikswo and F. Baudenbacher, *Anal. Chim. Acta*, 2003, **496**, 93–101.
6. A. Richardson, L. A. Schwerdtfeger, D. Eaton, I. McLean, C. S. Henry and S. A. Tobet, *Anal. Methods*, 2020, **12**, 297–303.
7. Z. Lin, T. Cherng-Wen, P. Roy and D. Trau, *Lab Chip*, 2009, **9**, 257–262.
8. S. Prill, M. S. Jaeger and C. Duschl, *Biomicrofluidics*, 2014, **8**, DOI:10.1063/1.4876639.
9. J. Zhu, J. He, M. Verano, A. T. Brimmo, A. Glia, M. A. Qasaimeh, P. Chen, J. O. Aleman and W. Chen, *Lab Chip*, 2018, **18**, 3550–3560.
10. Q. Zhou, D. Patel, T. Kwa, A. Haque, Z. Matharu, G. Stybayeva, Y. Gao, A. M. Diehl and A. Revzin, *Lab Chip*, 2015, **15**, 4467–4478.
11. J. L. Erkal, A. Selimovic, B. C. Gross, S. Y. Lockwood, E. L. Walton, S. McNamara, R. S. Martin and D. M. Spence, *Lab Chip*, 2014, **14**, 2023–2032.
12. S. A. N. Gowers, V. F. Curto, C. A. Seneci, C. Wang, S. Anastasova, P. Vadgama, G. Z. Yang and M. G. Boutelle, *Anal. Chem.*, 2015, **87**, 7763–7770.
13. I. C. Samper, S. A. N. Gowers, M. L. Rogers, D. S. R. K. Murray, S. L. Jewell, C. Pahl, A. J. Strong and M. G. Boutelle, *Lab Chip*, 2019, **19**, 2038–2048.
14. S. U. Hassan, A. M. Nightingale and X. Niu, *Analyst*, 2016, **141**, 3266–3273.
15. A. M. Nightingale, C. L. Leong, R. A. Burnish, S. ul Hassan, Y. Zhang, G. F. Clough, M. G. Boutelle, D. Voegeli and X. Niu, *Nat. Commun.*, 2019, **10**, 1–12.
16. A. Waldbaur, H. Rapp, K. Länge and B. E. Rapp, *Anal. Methods*, 2011, **3**, 2681–2716.
17. S. Waheed, J. M. Cabot, N. P. Macdonald, T. Lewis, R. M. Guijt, B. Paull and M. C. Breadmore, *Lab Chip*, 2016, **16**, 1993–2013.
18. L. H. Duong and P. C. Chen, *Biomicrofluidics*, 2019, **13**, 1–9.
19. S. Takenaga, B. Schneider, E. Erbay, M. Biselli, T. Schnitzler, M. J. Schöning and T. Wagner, *Phys. Status Solidi Appl. Mater. Sci.*, 2015, **212**, 1347–1352.

20. M. J. Beauchamp, G. P. Nordin and A. T. Woolley, *Anal. Bioanal. Chem.*, 2017, **409**, 4311–4319.
21. C. S. Carrell, C. P. McCord, R. M. Wydallis and C. S. Henry, *Anal. Chim. Acta*, 2020, **1124**, 78–84.
22. Y. Temiz, R. D. Lovchik, G. V. Kaigala and E. Delamarche, *Microelectron. Eng.*, 2015, **132**, 156–175.
23. C. S. Thompson and A. R. Abate, *Lab Chip*, 2013, **13**, 632–635.
24. X. Gong, X. Yi, K. Xiao, S. Li, R. Kodzius, J. Qin and W. Wen, *Lab Chip*, 2010, **10**, 2622–2627.
25. B. G. Chung, J. W. Park, J. S. Hu, C. Huang, E. S. Monuki and N. L. Jeon, *BMC Biotechnol.*, 2007, **7**, 1–7.
26. U. Y. Schaff, M. M. Q. Xing, K. K. Lin, N. Pan, N. L. Jeon and S. I. Simon, *Lab Chip*, 2007, **7**, 448–456.
27. A. Lamberti, A. Sacco, S. Bianco, E. Giuri, M. Quaglio, A. Chiodoni and E. Tresso, *Microelectron. Eng.*, 2011, **88**, 2308–2310.
28. A. Konda, J. M. Taylor, M. A. Stoller and S. A. Morin, *Lab Chip*, 2015, **15**, 2009–2017.
29. V. V. Abhyankar, M. Wu, C. Y. Koh and A. V. Hatch, *PLoS One*, 2016, **11**, 1–20.
30. E. Tkachenko, E. Gutierrez, M. H. Ginsberg and A. Groisman, *Lab Chip*, 2009, **9**, 1085–1095.
31. P. Occhetta, E. Biffi and M. Rasponi, in *Microfluidic and Compartmentalized Platforms for Neurobiological Research*, 2015, **103**, 25–38.
32. M. Rasponi, F. Piraino, N. Sadr, M. Laganà, A. Redaelli and M. Moretti, *Microfluid. Nanofluidics*, 2011, **10**, 1097–1107.
33. M. Rafat, D. R. Raad, A. C. Rowat and D. T. Auguste, *Lab Chip*, 2009, **9**, 3016–3019.
34. K. J. Klunder, Z. Nilsson, J. B. Sambur and C. S. Henry, *J. Am. Chem. Soc.*, 2017, **139**, 12623–12631.
35. K. E. Berg, Y. R. Leroux, P. Hapiot and C. S. Henry, *ChemElectroChem*, 2019, **6**, 4811–4816.

CHAPTER 4: CONCLUSION AND FUTURE DIRECTIONS

Since almost 95% of pharmaceutical drug candidates reaching clinical trials fail to gain market approval,¹ there is a clear need for physiologically relevant ex vivo organ models to bridge the gap between in vitro and in vivo. OOC technologies have overcome many of the limitations associated with traditional in vitro culture models by incorporating physiological fluid flow and, in some cases, multiple cell types. However, most OOC devices rely on cell lines which fail to truly capture the complex anatomy and physiology of organs in vivo. The intestines are a particularly important organ to model ex vivo because they play a central role in human health and disease² and is the primary organ that absorbs orally administered drugs.³ Designing a useful and reliable ex vivo intestinal model presents many challenges such as culturing viable explanted tissue for extended periods without blood supply, establishing and maintaining an oxygen gradient through the intestinal wall, and integrating sensors into microfluidic devices to detect physiological changes in real time. Perhaps the greatest challenge in designing an ex vivo intestinal model is maintaining diverse microbial populations on-chip that are representative of the adult human intestinal microbiome. Previous microfluidic intestinal models have included only a small subset of bacteria that inhabit the human gastrointestinal tract.⁴⁻⁹

This thesis describes the design and testing of 1) an instrumented microfluidic organotypic device (iMOD) for culture of murine intestinal tissue,¹⁰ and 2) a microfluidic sensor module to be implemented inline with the iMOD for real-time sensing of analytes and metabolites. In collaboration with Applied Medical Resources Corporation, we injection molded 200 iMODs that were used to culture full thickness murine intestinal explants for 72 hours ex vivo. Intestinal explants cultured in the iMOD formed a barrier between independent fluidic channels perfused with media, which is critical to recapitulating intestinal barrier function in vivo. We also

established differential oxygen concentrations in the fluidic channels and showed that more bacteria were present on the tissue's mucosal surface when exposed to near-anoxic media. While the kinds of bacteria cultured in the iMOD were not characterized, 16S sequencing will be utilized in future studies to investigate microbial diversity. We also designed and tested a reversibly sealed microfluidic sensor module that could be implemented downstream of the iMOD in experiments requiring additional sensors. Importantly, the sensor module can be easily disassembled, and both the sensors and microfluidic device can be cleaned and reused. Future work will include developing electrochemical/optical sensors for various biological compounds (i.e. glucose, lactate, butyrate) and integrating these sensors into the sensor module.

A crucial next step towards building a complete ex vivo intestinal model is to design and develop a scaled system comprising 1) pumps that supply culture media to multiple iMODs independently, 2) a custom manifold that holds multiple devices, 3) sensors to assess tissue health and monitor relevant analytes downstream of the explants in real-time, and 4) a fraction collector that stores effluent media in time resolved samples (Fig. 4.1). Thus far, we have designed initial prototypes of a multichannel peristaltic pump and a 48-well fraction collector. While several pump types have been implemented in OOC systems (i.e. pressure driven, syringe, gravity feed), peristaltic pumps are attractive because they are easily multiplexed, low cost, and enable flow rate control independent of a systems hydraulic resistance. However, peristaltic pumps often use silicone tubing that is highly oxygen permeable. A well-designed intestinal model requires near-anoxic media delivery to the mucosal surface of intestinal explants. Therefore, tubing material is a critical peristaltic pump design parameter when oxygen concentrations need to be controlled. Culture media that is perfused through the iMOD and sensors module will ultimately be stored in a fraction collector to be analyzed at the conclusion of experiments. As previously mentioned, the

fraction collector is necessary because many analytes of interest will be quantified off-chip using analytical techniques like mass spectrometry and nuclear magnetic resonance. Real-time monitoring of certain analytes is unnecessary, yet the fraction collector allows for time-resolved sampling of effluent media. The automated fraction collector would also enable experimenters to track shifts in the metabolome over time while reducing manual labor. The proposed iMOD system (Fig. 4.1) would address major limitations to current OOC systems such as scalability, usability, and online sensing. We anticipate that the proposed system will be used for both basic research (i.e. disease modeling) and testing of new oral drugs. Ultimately, this technology will be implemented in long-term studies to elucidate the relationship among microbial, epithelial, neuro and immune components of the intestinal wall in health and disease.

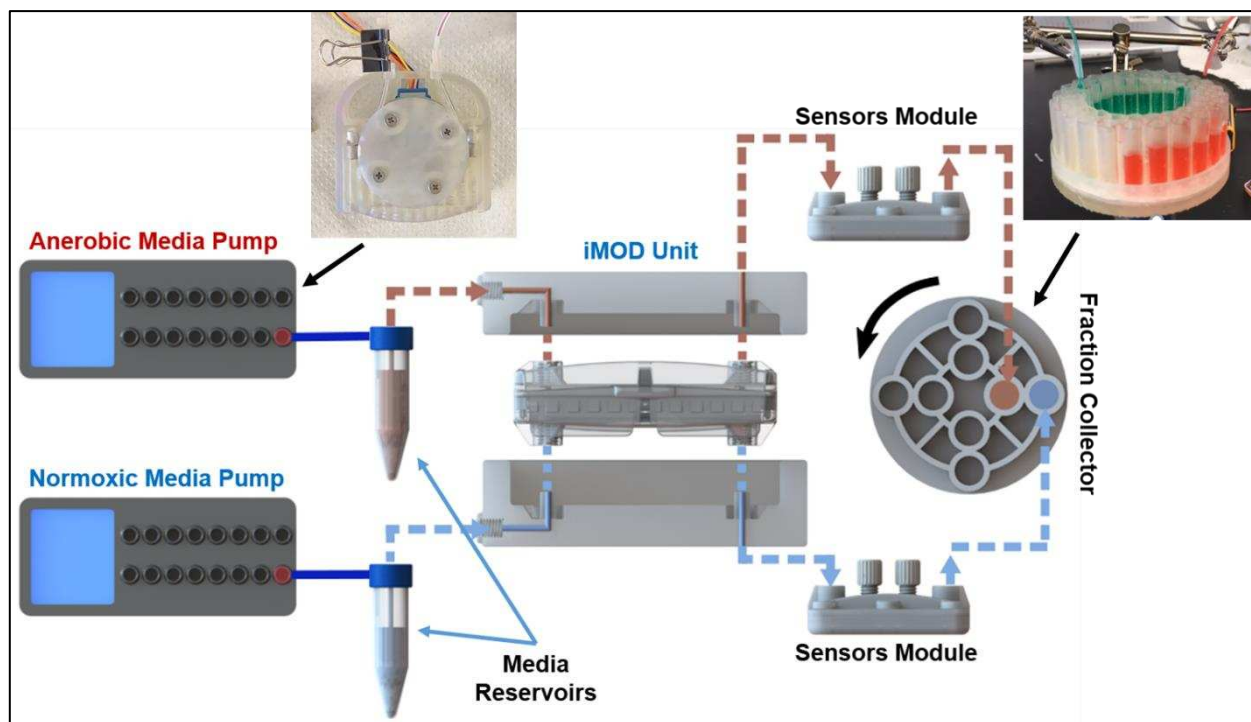


Figure 4.1 Scaled iMOD system consisting of anaerobic and normoxic media pumps, iMOD unit (device and manifold), sensors module, and fraction collector. Dashed lines indicate the direction of media flow (arrows) and corresponding oxygen concentration (color).

REFERENCES

1. A. A. Seyhan, *Transl. Med. Commun.*, 2019, **4**, 1–19.
2. S. Carding, K. Verbeke, D. Vipond, B. Corfe and L. Owen, *Microb. Ecol. Heal. Dis.*, 2015, **26**, 26191-.
3. Y. Masaoka, Y. Tanaka, M. Kataoka, S. Sakuma and S. Yamashita, *Eur. J. Pharm. Sci.*, 2006, **29**, 240–250.
4. H. J. Kim, D. Huh, G. Hamilton and D. E. Ingber, *Lab Chip*, 2012, **12**, 2165–2174.
5. W. Shin, A. Wu, M. W. Massidda, C. Foster, N. Thomas, D.-W. Lee, H. Koh, Y. Ju, J. Kim and H. J. Kim, *Front. Bioeng. Biotechnol.*, 2019, **7**, 1–13.
6. P. Shah, J. V. Fritz, E. Glaab, M. S. Desai, K. Greenhalgh, A. Frachet, M. Niegowska, M. Estes, C. Jäger, C. Seguin-Devaux, F. Zenhausem and P. Wilmes, *Nat. Commun.*, 2016, **7**, DOI:10.1038/ncomms11535.
7. H. J. Kim, H. Li, J. J. Collins and D. E. Ingber, *Proc. Natl. Acad. Sci. U. S. A.*, 2016, **113**, E7–E15.
8. S. Jalili-Firoozinezhad, F. S. Gazzaniga, E. L. Calamari, D. M. Camacho, C. W. Fadel, A. Bein, B. Swenor, B. Nestor, M. J. Cronce, A. Tovaglieri, O. Levy, K. E. Gregory, D. T. Breault, J. M. S. Cabral, D. L. Kasper, R. Novak and D. E. Ingber, *Nat. Biomed. Eng.*, 2019, **3**, 520–531.
9. M. Marzorati, B. Vanhoecke, T. De Ryck, M. S. Sadabad, I. Pinheiro, S. Possemiers, P. Van Den Abbeele, L. Derycke, M. Bracke, J. Pieters, T. Hennebel, H. J. Harmsen, W. Verstraete and T. Van De Wiele, *BMC Microbiol.*, 2014, **14**.
10. A. Richardson, L. A. Schwerdtfeger, D. Eaton, I. McLean, C. S. Henry and S. A. Tobet, *Anal. Methods*, 2020, **12**, 297–303.

Bridging the Gap: A Microfluidic Device for Studying Organotypic Barrier Tissues

Summary

Organ and tissue-on-a-chip technologies are powerful tools for drug discovery and disease modeling. However, many of these systems were not designed to recapitulate the intricate structure and function of native tissues. We developed a microfluidic device that supports full-thickness murine intestinal explants up to 72 h while maintaining differential oxygen across the tissue. The explants retained barrier properties for the duration of experiments, indicated by minimal trans-tissue dye transfer. Further, we observed increased mucosal bacterial presence in explants cultured in a low oxygen environment. Incorporating cellularly heterogeneous tissue into microfluidic devices with physiologically relevant environments is a key step in bridging the gap between in vitro and in vivo.

Introduction

Current Tissue-on-a-chip systems rely heavily on in vitro cell culture to create reductionist models of tissues and organs [1-3]. These systems recapitulate some tissue functions and are useful for high-throughput screening but fail to capture the richness of cell interactions of tissues in vivo because they lack the cellular diversity and complex architecture of native tissue. To bridge the gap between in vitro and in vivo models, some have incorporated tissue explants into microfluidic devices [4-7]. Progress has been made for many tissues, but integration of intestinal tissue into microfluidic devices ex vivo has remained challenging because it requires creating an oxygen gradient across the tissue to faithfully recreate the in vivo environment. Here, we report a

microfluidic device that supports differential flow with physiologically relevant oxygen concentrations over intestinal explants.

Experimental

Instrumented microfluidic organotypic device (iMOD) prototypes were made using injection molding and consist of three cyclic olefin copolymer (COC) layers separated by polyurethane gaskets (Figure 1A). Intestinal tissue explants are housed in the middle layer with the mucosa and serosa facing independent microfluidic channels. Devices are assembled by stacking layers and snapping them together via integrated snap-fit fasteners. Glass coverslips fixed above and below the tissue enable on-chip imaging (Figure 1C,D) and visualization (Figure 1B). Dissolved oxygen concentrations (DOC) were measured using oxygen sensor spots adhered within

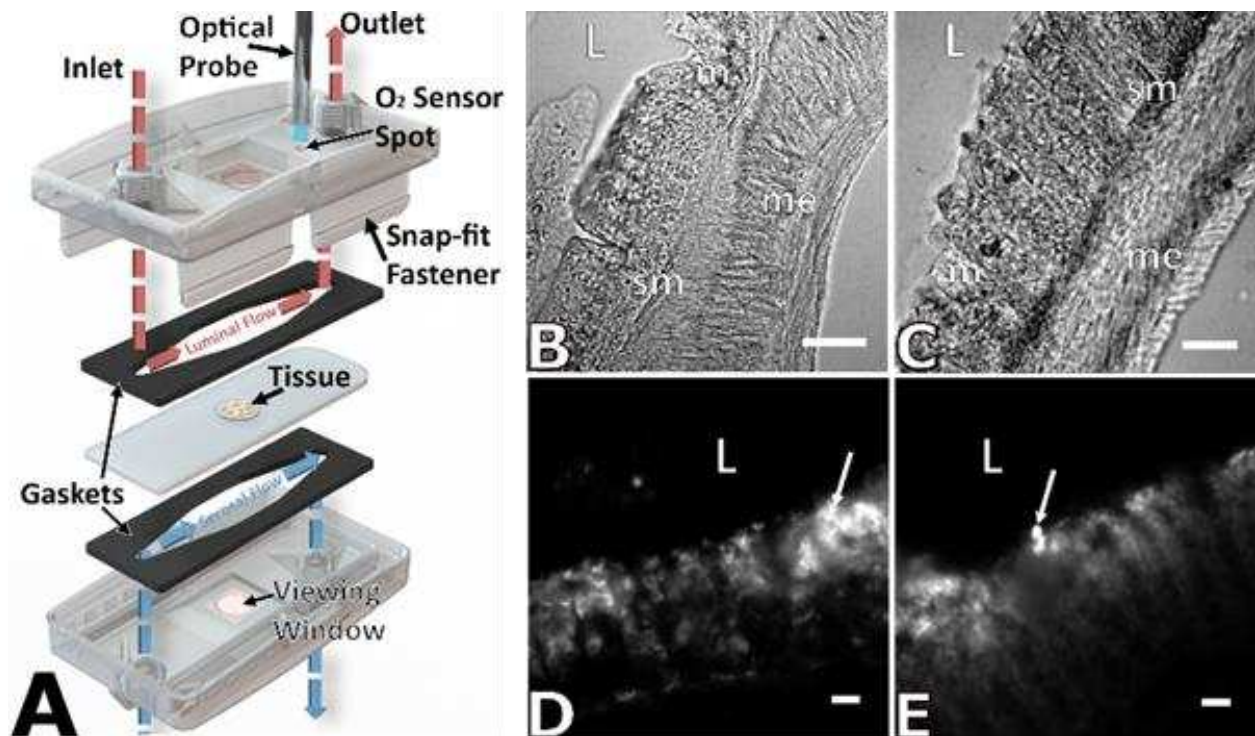


Figure A1. Schematic illustration of the iMOD design and analysis of tissue health. (A) an exploded model of the iMOD system showing luminal (red) and serosal (blue) flow paths. B-C show stereotypic anatomical arrangement of gut wall at 0 h (B) and 72 h in low oxygen (C). D-E demonstrates stereotypic EtHD signal in colonic explants at apical most aspect of colonic crypts (arrows) at 0h (D) and 72 h in low oxygen (E). 'L' denotes intestinal lumen, 'm' indicates mucosa, 'sm' submucosa, and 'me' muscularis externa. Scale bars in A and B are 100 μm , scale bar in C is 50 μm , and scale bars in D-F are 25 μm .

the device (fluorescent quenching). Serum-free media was perfused in each channel at 250 $\mu\text{L/hr}$, to provide low shear stress across the tissue.

Results and Discussion

Mouse colon explants were cultured in the iMOD for 72 h *ex vivo* in both ambient and low mucosal DOC, maintaining intact tissue architecture, as marked by patterned rows of colonic crypts, interspersed lamina propria, and stereotypic arrangement of underlying submucosal and muscular layers (Figure 1B,C). Seen in Figure 1D,E, minimal cell death was observed, indicated by ethidium homodimer staining. Figure 2 shows that culture media perfused in each channel remained separated over 72 h, as demonstrated by the lack of fluorescein leakage across the tissue. Verification of media separation demonstrated that tissue explants maintained a physical barrier.

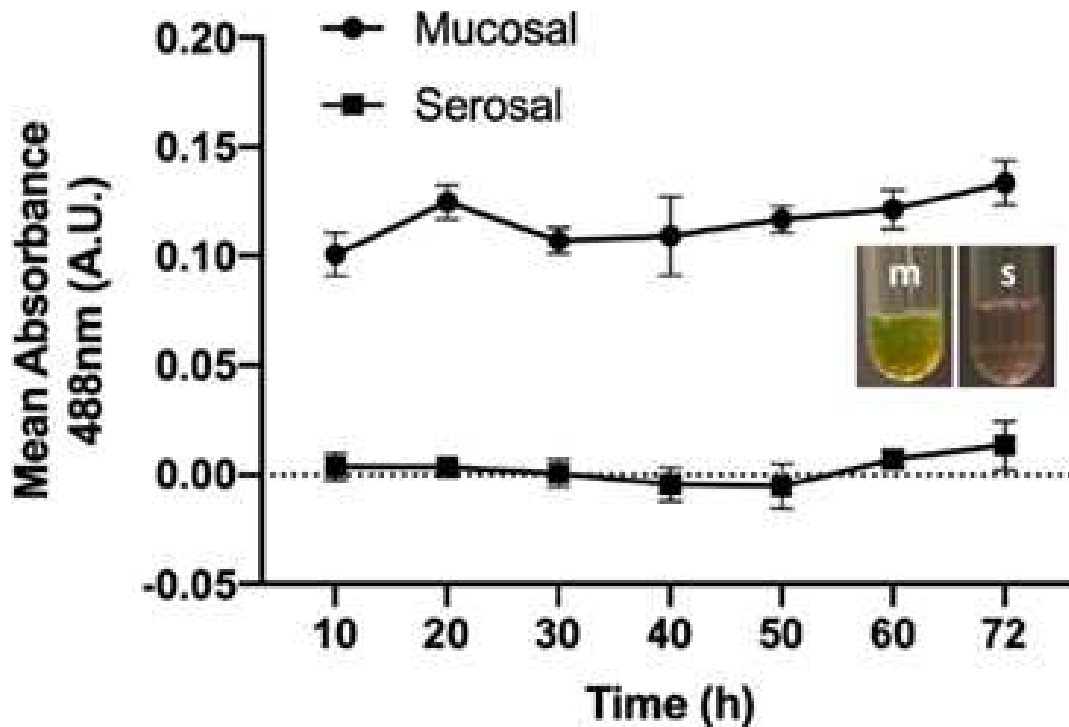


Figure A2. Media was separated across channels as marked by fluorescein absorbance in effluent media. Mean absorbance (A.U.) at 488 nm wavelength demonstrates significantly more fluorescein presence in mucosal (circular points) effluents compared to serosal (square points) ($P < 0.001$). No significant differences were observed across time in either the mucosal ($P > 0.20$) or serosal ($P > 0.45$) effluents. All statistical analyses were performed using a one-way ANOVA with $\alpha = .05$. Representative images show visible green in mucosal (m) effluent compared to serosal (s) effluent.

We also demonstrated differential maintenance of bacteria on the tissue's mucosal surface as a function of DOC (Figure 3). Fluorescent gram stain revealed increased bacterial presence on tissue perfused with media containing low DOC versus ambient DOC. To the authors' knowledge, no other group has investigated differences in intestinal microbiota maintenance as a function of DOC in a microfluidic device. Ultimately, the iMOD supplemented with additional sensing functions will be implemented in long-term studies to elucidate the relationship among microbial, epithelial, neuro and immune components of the gut wall in health and disease.

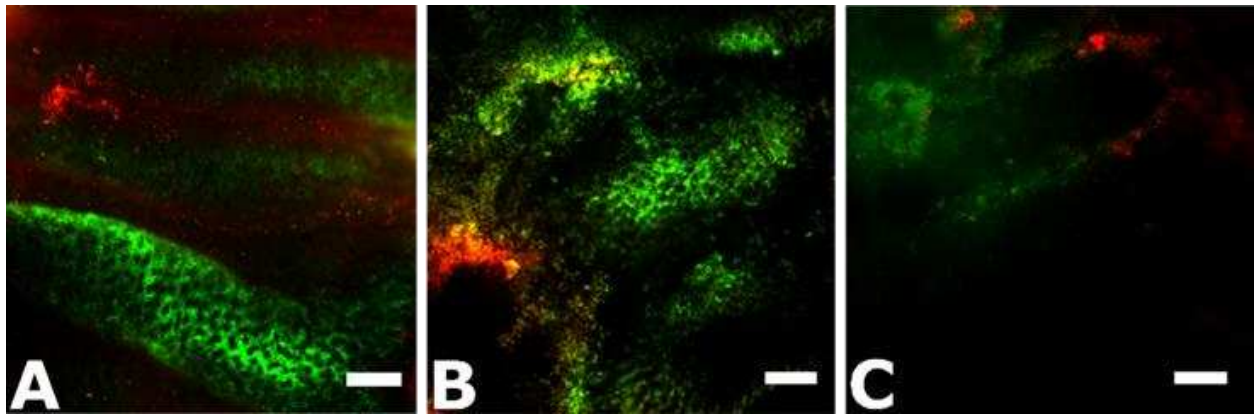


Figure A3 Native microbiota were maintained in iMOD, and more bacteria were visible in an explant cultured in lower oxygen conditions. (A) Baseline bacterial levels are shown at 0h ex vivo via hexidium iodide (7.05 μM) fluorescence in red, signifying Gram-positive bacteria, and SYTO9 (5.01 μM) fluorescence in green, signifying Gram-negative bacteria. Gram stain fluorescence was noticeably higher in tissue cultured in lowered oxygen conditions (B; 3 mmHg) when compared to tissue cultured in ambient oxygen (C; 100 mmHg) containing media. Scale bars in all panels are 100 μm .

REFERENCES

- [1] Kasendra et. al., *Sci. Rep.*, 2018, **8**, 1–14. [2] Shah et. al., *Nat. Commun.*, 2016, **7**, DOI:10.1038/ncomms11535. [3] Shin et. al., *Front. Bioeng. Biotechnol.*, 2019, **7**:13. [4] Astolfi et. al., *Lab Chip*, 2016, **16**, 312–325. [5] Xiao et. al., *Nat. Commun.*, 2017, **8**, 1–13. [6] Shim et. al., *Lab Chip*, 2019, **19**, 1013–1026. [7] Tedjo et. al., *Biosens. Bioelectron.*, 2018, **114**, 78–88.

APPENDIX B: COMPUTATIONAL MODEL OF INTESTINAL OXYGEN TRANSPORT WITHIN A MICROFLUIDIC ORGANOTYPIC DEVICE

Introduction

The *in vivo* intestinal environment features a steep oxygen gradient from lumen to serosa, which is essential for anaerobic bacteria and host tissue to survive. In the absence of blood flow, cultured intestinal explants require oxygen delivery via diffusion and convective transport in surrounding media. Previously, we cultured full thickness (~750 μm) murine intestinal explants in a microfluidic organotypic device (MOD) by perfusing media with low and ambient oxygen concentrations across mucosal and serosal surfaces, respectively.¹ Here, we employ computational simulation to investigate oxygen distribution and consumption within intestinal tissue cultured in the MOD as a function of media flow rates and oxygen concentrations. These results, and those from future studies will influence design parameters for future MOD iterations such as channel dimensions and maximum tissue thickness.

Methods

A 3D computational model was created in COMSOL Multiphysics 4.4 by coupling the Laminar Flow and Transport of Diluted Species modules. Fluid flow was governed by the steady-state Navier-Stokes equations (eq. 1 and 2) assuming a Newtonian, incompressible fluid.

$$\rho(\mathbf{u} \cdot \nabla)\mathbf{u} = \nabla \cdot \left[-p\mathbf{I} + \mu(\nabla\mathbf{u} + (\nabla\mathbf{u})^T) \right] + \mathbf{F} \quad (1)$$

$$\rho\nabla \cdot \mathbf{u} = 0 \quad (2)$$

Here, \mathbf{u} is the fluid velocity field, ρ is density, p is pressure, μ is dynamic viscosity, \mathbf{F} is body forces, and ∇ is the del operator. Oxygen transport was governed by the steady-state convection-diffusion equation (eq. 3) with a reaction term to account for tissue oxygen consumption. Here, \mathbf{D}_i

is the diffusion coefficient, c_i is species concentration, and R_i is a reaction term. The convective velocity field (\mathbf{u}) in eq. 3 was coupled to the velocity field calculated in the Laminar Flow module. In other words, convective oxygen transport resulted from fluid flow in the channels. Tissue oxygen consumption was modeled as a function of local oxygen concentration assuming first-order Michaelis-Menten kinetics (eq. 4). Here, R_i is the oxygen consumption rate, R_{max} is the maximum oxygen consumption rate, $[c]$ is species concentration, K_m is the Michaelis-Menten constant, and $step(c)$ is a step function that terminates oxygen consumption when local concentrations fall below a specified value. Figure 4 shows the model schematic with corresponding physics in each domain.

$$\nabla \cdot (-D_i \nabla c_i) + \mathbf{u} \cdot \nabla c_i = R_i \quad (3)$$

$$R_i = \frac{R_{max}[c]}{[c] + K_m} * step(c) \quad (4)$$

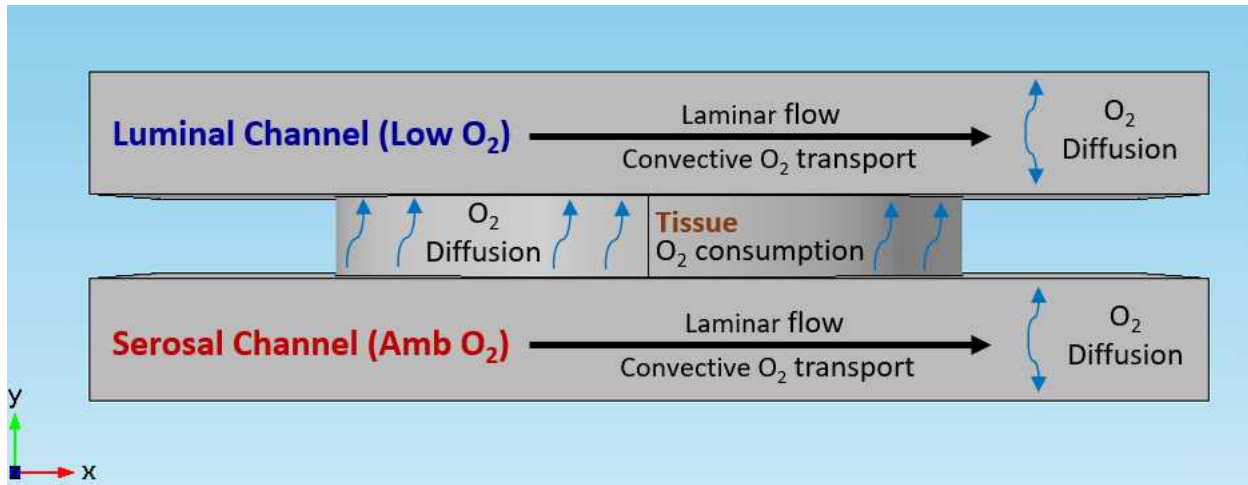


Figure B1 Schematic of oxygen transport and fluid flow in the iMOD. Laminar flow, convective and diffusive oxygen transport occur in the fluid channels whereas diffusive oxygen transport and oxygen consumption occur in the tissue explant.

Boundary/Initial Conditions and Model Parameters

Two boundary conditions were applied to the fluid inlets: 1) laminar inflow with flow rates that ranged from 2.5-10 mL/h, and 2) mass inflow of dissolved oxygen at a concentration of 20% for the serosal channel and 0.5-2.5% for the luminal channel. Two boundary conditions were also applied to the fluid outlets: 1) laminar outflow with an exit pressure of 1 atm, and 2) mass outflow. A no flux boundary condition was applied to all other surfaces excluding the tissue-channel interfaces. Initial oxygen concentrations for the tissue, serosal channel, and luminal channel were 7%, 20%, and 0.5-2.5%, respectively. Model parameters are summarized in Table 1.

Table B1 Model parameter values

Parameter	Description	Value
D_{media}	O ₂ diffusion coefficient in culture media (37° C)	3.15×10^{-9} [m ² /s]
D_{tissue}	O ₂ diffusion coefficient in intestinal tissue	2.0×10^{-9} [m ² /s]
R_{max}	Max O ₂ consumption rate	- 0.001 [mol/m ³ /s]
K_m	Michaelis-Menten constant	0.011 [mol/m ³]
C_{off}	O ₂ concentration at which O ₂ consumption is terminated	0.001 [mol/m ³]
ρ_{tissue}	Density of intestinal tissue	1088 [kg/m ³]
ρ_{media}	Density of culture media (37° C)	993 [kg/m ³]
μ	Dynamic viscosity of culture media (37° C)	6.9×10^{-4} [Pa.s]

Results and Discussion

As shown in Figure 2, higher flow rates resulted in a steeper oxygen gradient within the tissue due to convective oxygen transport to the tissue's serosal surface. For all flow rates, dissolved oxygen concentrations (DOC) in the Luminal and Serosal channels were set at 0.5% and

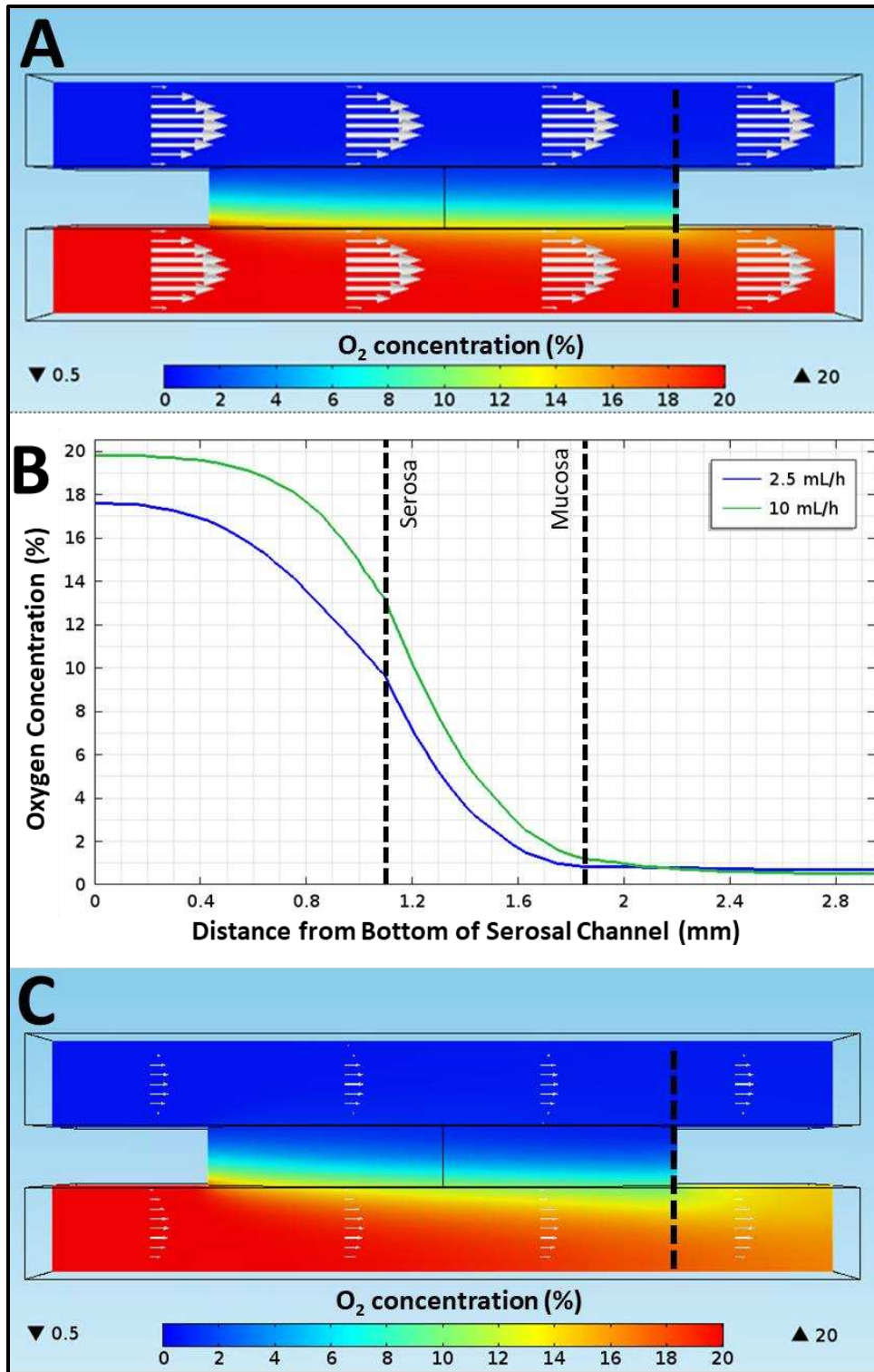


Figure B2 Oxygen concentration profiles with varying Luminal (upper channel, 0.5% O₂) and Serosal (lower channel, 20% O₂) media flow rates. A) Flow rate = 2.5mL/h. B) Tissue O₂ concentration with flow rates of 2.5 mL/h and 10 mL/h. C) Flow rate = 10mL/h. Arrows show direction and magnitude of velocity; dashed vertical lines in A and C show location where data for B was obtained.

20%, respectively. DOC at the serosal surface, center of the tissue, and mucosal surface were [9.6%, 2.8%, 0.84%] and [13%, 4.5%, 1.2%] for flow rates equal to 2.5 mL/h and 10 mL/h, respectively. The differences in DOC between flow rates were most pronounced at the tissue's serosal surface because most of the oxygen that diffused through the tissue was consumed before reaching the tissue's mucosal surface. In vivo, intestinal oxygen concentrations are ~7-10% in the muscular wall,² ~ 6% in the vascularized submucosa,² and < ~2% in the epithelial cell layer (Zheng 2015). While a flow rate of 10 mL/h resulted in a higher than average serosal DOC, the submucosal and mucosal DOC more closely reflected in vivo conditions.

We also computed the tissue oxygen gradient as a function of luminal DOC. In this study, both the luminal (0.5%, 1.5%, 2.5% O₂) and serosal (20% O₂) channels were perfused at a flow rate of 10 mL/h. Illustrated in Figure 3, DOC at the serosal surface, center of the tissue, and mucosal surface were [13%, 4.5%, 1.2%], [13%, 4.9%, 1.9%], and [13%, 5.2%, 2.6%] for luminal DOC of 0.5%, 1.5%, and 2.5%, respectively. As expected, the difference in DOC were greatest at the tissue's mucosal surface because only the luminal DOC was varied. While mucosal DOC were higher with increased luminal DOC, anaerobic bacteria require near-anoxic conditions to survive. Therefore, 1.5% and 2.5% Luminal DOC may be unsuitable for culturing diverse microbial populations in the iMOD. One limitation of this model is that oxygen consumption by obligate aerobes, facultative anaerobes, and microaerophiles inhabiting the luminal channel is not accounted for. Future studies may indicate that bacterial oxygen consumption in the luminal channel necessitates perfusion of media with higher DOC.

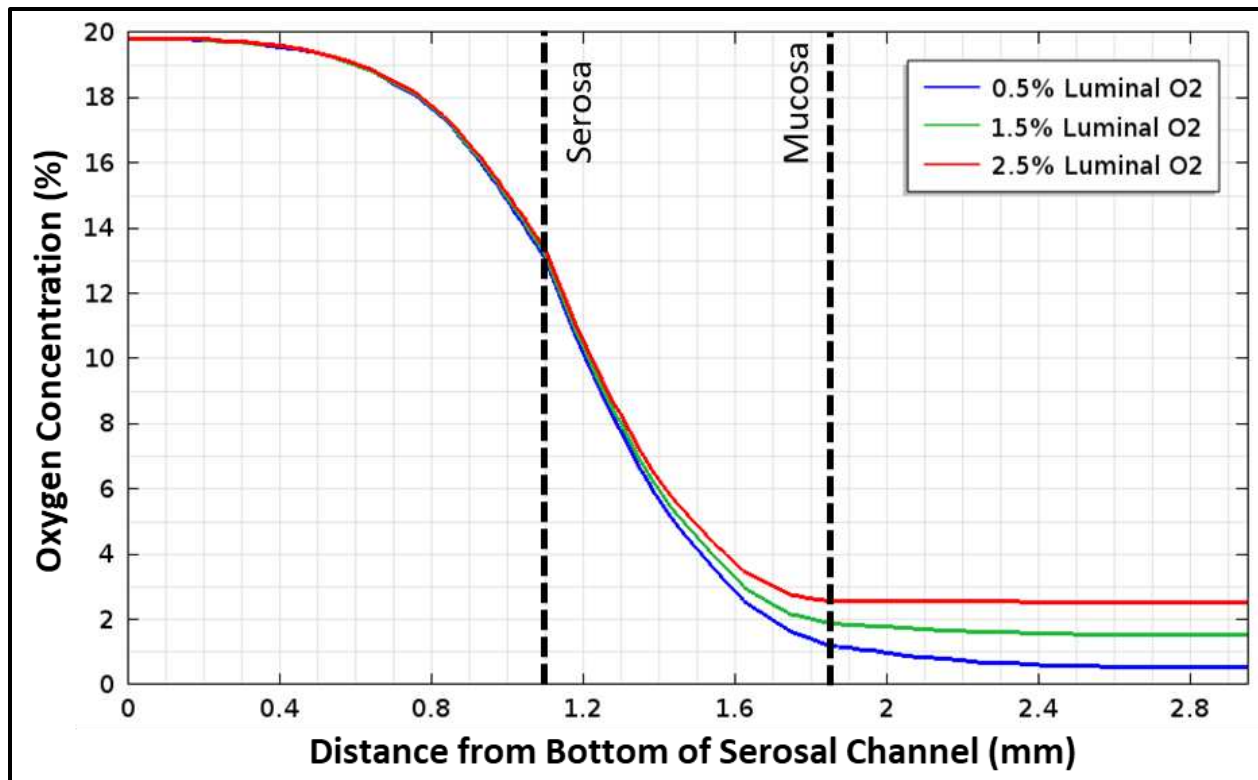


Figure B3 Tissue oxygen gradients as a function of luminal dissolved oxygen concentration. Dashed lines indicate the serosal and mucosal surfaces of the tissue. Flow rate = 10 mL/h.

Conclusion

Future extensions of this model could include parameterizing channel dimensions, serosal DOC, tissue thickness, and tissue oxygen consumption rates. Additionally, bacterial oxygen consumption in the luminal channel could be accounted for. Long term, the iMOD will be used to study interactions among the microbial-epithelial-immune-neural components that comprise the barrier along the gastrointestinal tract. Future modeling experiments will help dictate the parameters of tissue explant studies performed using the iMOD.

References

- [1] Richardson et al., *Anal. Methods*, 2020, **12**, 297-303. [2] Schwerdtfeger et al., *PLoS ONE*, 2019, **14**. [3] Zheng et al., *Am J Physiol Cell Physiol.*, 2015, **309**, 350-360